NEUROSCIENCE

Adolescence is a sensitive period for prefrontal microglia to act on cognitive development

Sina M. Schalbetter[1], Anina S. von Arx[1], Natalia Cruz-Ochoa[2], Kara Dawson[1], Andranik Ivanov[3], Flavia S. Mueller[1], Han-Yu Lin[1], René Amport[1], Wiebke Mildenberger[4], Daniele Mattei[1,5], Dieter Beule[3,6], Csaba Földy[2,7], Melanie Greter[4], Tina Notter[1,8], Urs Meyer[1,7]*

The prefrontal cortex (PFC) is a cortical brain region that regulates various cognitive functions. One distinctive feature of the PFC is its protracted adolescent maturation, which is necessary for acquiring mature cognitive abilities in adulthood. Here, we show that microglia, the brain's resident immune cells, contribute to this maturational process. We find that transient and cell-specific deficiency of prefrontal microglia in adolescence is sufficient to induce an adult emergence of PFC-associated impairments in cognitive functions, dendritic complexity, and synaptic structures. While prefrontal microglia deficiency in adolescence also altered the excitatory-inhibitory balance in adult prefrontal circuits, there were no cognitive sequelae when prefrontal microglia were depleted in adulthood. Thus, our findings identify adolescence as a sensitive period for prefrontal microglia to act on cognitive development.

INTRODUCTION

The prefrontal cortex (PFC) is the cortical region of the anterior pole of the mammalian brain (*1*). It provides executive "top-down" control pertaining to various cognitive processes, including decision-making and goal-directed behavior, attention, cognitive flexibility, and working memory (*1*, *2*). One distinctive feature of the PFC is its protracted maturation, which is sustained throughout adolescence until early adulthood and necessary for acquiring mature cognitive abilities (*3*–*5*). Thus, the PFC is recognized as being the last brain region to reach full maturity in humans (*6*) and in other species, including rodents (*5*). During postnatal maturation, the PFC undergoes substantial refinement of neuronal circuitries and synaptic connections, which, in turn, adapts prefrontal circuits to respond optimally to the changing demands occurring during the transition from adolescence to adulthood (*3*–*5*). Disturbances in PFC structures and functions are also strongly associated with major psychiatric disorders, especially with those that typically emerge in late adolescence or early adulthood, such as schizophrenia and bipolar disorder (*7*–*9*).

Synaptic refinement is increasingly recognized to involve the dynamic actions of microglia, which are the resident immune cells of the brain parenchyma (*10*). Microglia cells arise from erythromyeloid progenitor cells in the yolk sac, colonize the brain during early fetal development, and retain the capacity for self-renewal in the adult brain (*10*). Under physiological conditions, they account for 5 to 12% and 0.5 to 15% of the total cell population in the adult mouse (*11*) and human (*12*) brain, respectively. Besides their classical immunological functions, microglia contribute to the remodeling of brain circuitries and synaptic connections through phagocytic (*13*, *14*) and nonphagocytic (*15*, *16*) mechanisms. While microglia have been shown to mediate synaptic refinement in numerous brain areas (*13*–*17*), including the PFC (*18*), it remains unknown whether they shape the development of mature cognitive abilities pertaining to adult PFC functions. Therefore, we sought to establish a model system that would allow us to investigate the relative contribution of microglia to the structural and functional maturation of the PFC in mice. While several genetic and pharmacological models for cell-specific microglia manipulations exist (*19*–*24*), we opted for an approach that would enable us to manipulate microglia selectively in the PFC during a restricted time window without inducing nonspecific effects on peripheral immune cells or other cells of the central nervous system. Thus, we deemed stereotaxic injection of clodronate disodium salt (CDS), which induces selective apoptosis of microglia through inhibition of their mitochondrial adenosine 5′-diphosphate/adenosine 5′-triphosphate (ATP) translocase (*24*, *25*), the most suitable method to deplete microglia selectively and transiently from the PFC during adolescence. Using this transient loss-of-function approach, we show that depletion of prefrontal microglia in adolescence is sufficient to induce lasting changes in PFC-associated cognitive functions and synaptic structures.

RESULTS

A model for cell-specific and transient depletion of prefrontal microglia

To explore their role in the structural and functional maturation of the PFC, we transiently depleted microglia from the PFC during a defined window of adolescence (fig. S1). This was achieved using a single, bilateral stereotaxic injection of CDS into the medial portion of the PFC at 6 weeks of age (fig. S1). We selected this adolescent time period because it represents a critical window of synaptic refinement and dendritic remodeling in the maturing PFC (*3*–*5*, *26*). Furthermore, this time period temporally coincides with increased prefrontal expression of microglia-defining genes and complement component 3 (C3) (fig. S2), the latter of which has been implicated in complement-dependent synaptic remodeling by microglia (*13*).

[1]Institute of Pharmacology and Toxicology, University of Zürich-Vetsuisse, Zürich, Switzerland. [2]Laboratory of Neural Connectivity, Faculties of Medicine and Natural Sciences, Brain Research Institute, University of Zürich, Zürich, Switzerland. [3]Core Unit Bioinformatics, Berlin Institute of Health, Charité-Universitaetsmedizin, Berlin, Germany. [4]Institute of Experimental Immunology, University of Zürich, Zürich, Switzerland. [5]Department of Neurology, Icahn School of Medicine at Mount Sinai, New York, NY, USA. [6]Max Delbrück Center for Molecular Medicine in the Helmholtz Association (MDC), Berlin, Germany. [7]Neuroscience Center Zürich, Zürich, Switzerland. [8]Neuroscience and Mental Health Research Institute, Cardiff University, Cardiff, Wales, UK.
*Corresponding author. Email: urs.meyer@vetpharm.uzh.ch

Compared to control mice undergoing sham surgery or control mice receiving a bilateral stereotaxic injection of phosphate-buffered saline (PBS), CDS-injected mice exhibited a transient reduction in ionized calcium-binding adaptor molecule 1–positive ($Iba1^+$) microglial cell numbers in the PFC spanning the infralimbic (IL), prelimbic (PL), and anterior cingulate (AC) cortices (Fig. 1, A and B). The CDS-induced microglia depletion started to emerge at 1 day post-injection (1 dpi), peaked at 5 dpi, and normalized as of 10 dpi (Fig. 1A). Intra-PFC injection of CDS also led to a transient decrease in microglia density in the secondary motor cortex but not in the primary motor cortex, primary somatosensory cortex, and forceps minor of the corpus callosum regions (fig. S3). The intra-PFC CDS injection did not change the density of prefrontal neurons or astrocytes (fig. S4), showing that our experimental approach selectively depleted prefrontal microglia while sparing other major cell types.

To examine whether the stereotaxic surgery may cause an infiltration of peripheral immune cells to the PFC, we prepared single-cell suspension of prefrontal tissue at the peak of CDS-induced microglia depletion (5 dpi) and quantified the numbers of peripheral immune cells in the PFC using flow cytometry. This analysis showed that the numbers of $CD4^+$ and $CD8^+$ T cells (pregated on $CD45^{hi}$ $MHCII^-CD11b^-$), neutrophils ($CD45^{hi}CD11b^+Ly6G^+$), and $Ly6C^{hi}$ monocytes ($CD45^{hi}CD11b^+Ly6G^{hi}$) in the PFC were generally low and did not differ between mice receiving a bilateral stereotaxic

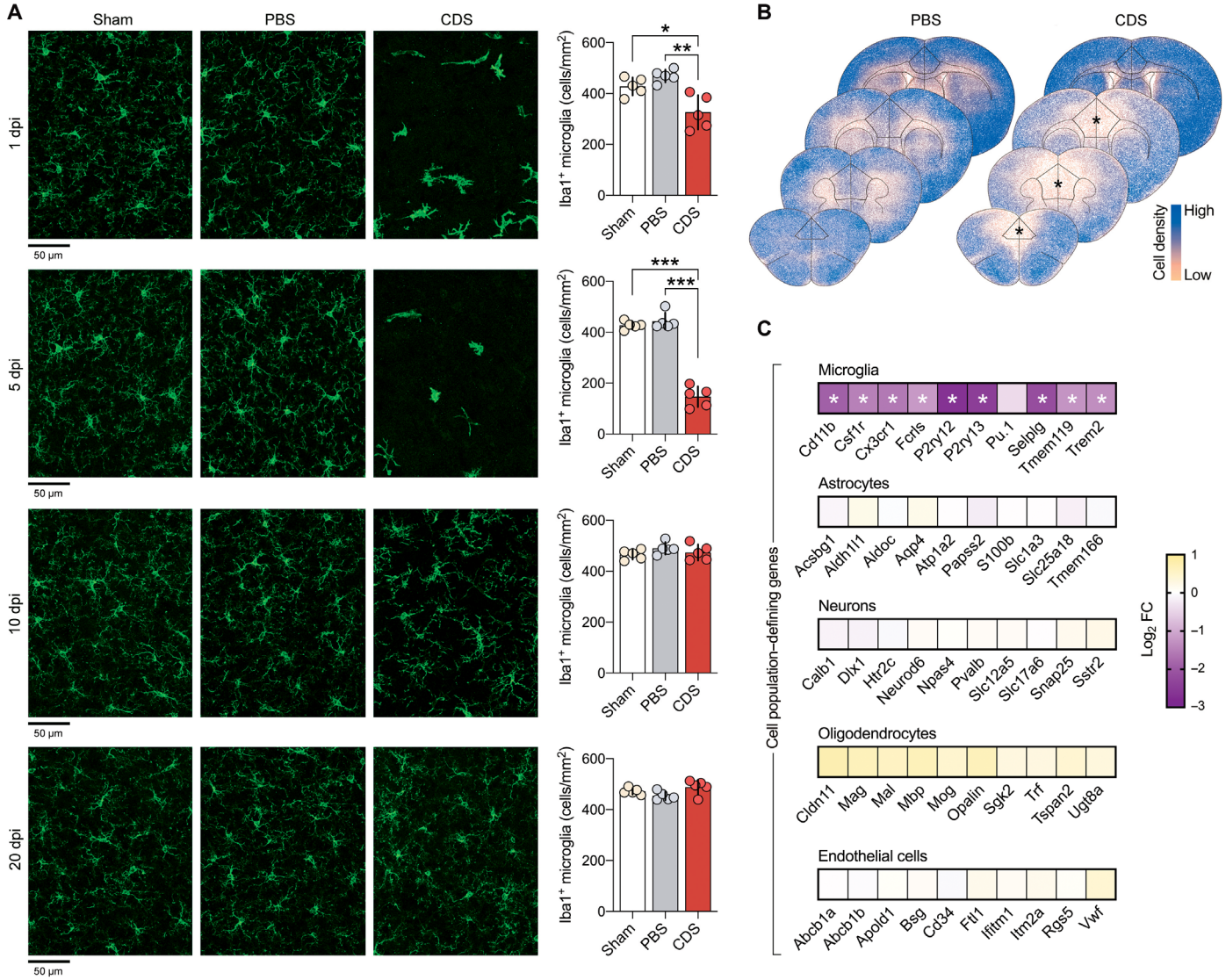

Fig. 1. Effectiveness, transiency, and selectivity of CDS-induced microglia depletion in the PFC of adolescent mice. (**A**) Representative images of $Iba1^+$ microglia (green) in the medial PFC of adolescent mice receiving sham surgery or bilateral intra-PFC injection of PBS or CDS. The images were taken 1, 5, 10, and 20 days post-injection (dpi). The bar graphs show the number of $Iba1^+$ microglia in the medial PFC at different dpi intervals. $^*P < 0.05$, $^{**}P < 0.01$, and $^{***}P < 0.001$ [post hoc tests following ANOVA at 1 dpi: $F_{(2,12)} = 12.7$, $P < 0.01$; at 5 dpi: $F_{(2,12)} = 140.5$, $P < 0.001$]; $N = 5$ mice per group and dpi. (**B**) Color-coded overlays of coronal PFC sections taken from five mice per group (PBS or CDS), wherein each dot represents an $Iba1^+$ microglial cell. Note the reduction of microglial cell density in the medial portion of PFC of CDS mice, as indicated by the symbol (*). (**C**) Expression of genes [$\log_2$ fold change (FC)] defining microglia, astrocytes, neurons, oligodendrocytes, and endothelial cells in CDS relative to PBS mice at 5 dpi; significantly altered genes are denoted with the symbol (*), based on FDR $q < 0.05$, as provided in fig. S6 and table S1; $N = 5$ mice per group.

injection of PBS or CDS and mice receiving no stereotaxic injection (sham control mice) (fig. S5). These data demonstrate that the surgical manipulation did not induce a potential bias resulting from peripheral immune cell infiltration into the PFC.

To further ascertain the cellular selectivity of intra-PFC administration of CDS, we conducted next-generation RNA sequencing (RNA-seq) of bulk PFC tissue from CDS- or PBS-injected mice, which was extracted during the peak of microglia depletion (5 dpi). Using a false discovery rate (FDR) threshold of $q < 0.05$, we identified 647 down-regulated and 560 up-regulated genes in CDS-injected mice relative to PBS controls (fig. S6). As expected, microglia-defining genes (Fig. 1C, fig. S6, and table S1) and genes pertaining to inflammatory immune responses (fig. S7) were among the most strongly down-regulated genes in CDS-injected mice during the acute phase of microglia depletion. CDS did not alter the expression of genes that define other major cell populations, including neurons, astrocytes, oligodendrocytes, or endothelial cells (Fig. 1C and table S1). To ascertain the transiency of the transcriptional effects of the adolescent microglia depletion, we performed the same RNA-seq analysis using PFC tissue of adult (12-week-old) mice injected with PBS or CDS in adolescence. At this age, 20 and 19 genes were down- and up-regulated, respectively, in CDS relative to PBS mice (table S2). Contrary to its post-acute effects (Fig. 1C and table S1), CDS treatment in adolescence did not alter microglia-defining genes in adulthood (table S3). Consistent with the bulk RNA-seq data generated in 12-week-old mice, quantifying microglia-defining genes in microglia isolated from the adult PFC via magnetic-activated cell sorting (MACS) showed no microglia-related transcriptional differences between CDS and PBS mice at the time when microglia were fully repopulated in CDS-injected mice (fig. S8). Together, these data demonstrate that a single, bilateral intra-PFC injection of CDS in 6-week-old mice is suitable to induce a cell-specific and transient depletion of prefrontal microglia in adolescence.

Adult cognitive deficits after transient prefrontal microglia deficiency in adolescence

In a next step, we examined whether behavioral and cognitive development is influenced by prefrontal microglia deficiency in adolescence. To this aim, 6-week-old mice were subjected to intra-PFC CDS or PBS injections, after which they were allowed to develop until adulthood (fig. S1). Adult behavioral testing commenced at 12 weeks of age and included tests that critically depend on PFC functions, including social approach behavior and social recognition memory (*27*), temporal order memory (*28*), and extinction of contextual fear (*29*). In the social interaction test, in which adult PBS and CDS mice were first allowed to freely explore a nonfamiliar mouse or dummy object (phase 1), both groups displayed a clear preference toward the nonfamiliar mouse, indicating intact social approach behavior in either group (Fig. 2A). When allowed to explore a novel versus familiar mouse in phase 2 of the test, only PBS mice showed a preference toward the novel mouse (Fig. 2A). In contrast, CDS mice were unable to discriminate between the novel and familiar mouse (Fig. 2A), demonstrating impaired social recognition memory in this group (*27*). Consistent with the latter deficit, adult CDS mice also displayed an impairment in temporal order memory for objects (Fig. 2B). In the temporal order memory test, PBS and CDS mice were first allowed to freely explore a first pair of identical objects (sample phase 1) and then a novel pair of identical objects (sample phase 2). In the subsequent test phase, when the mice were allowed to choose between one object from the first pair (temporally remote objects) and one from the second pair (temporally recent objects), only PBS mice showed a preference toward the temporally remote object, whereas CDS mice failed to discriminate between the two objects (Fig. 2B). Additional analyses of the relative amount of time exploring the objects in sample phases 1 and 2 of the temporal order memory test revealed no effects of CDS on object exploration per se (Fig. 2B), suggesting that the CDS-induced disruption of temporal order memory represents a genuine deficit in the capacity of CDS mice to discriminate the relative recency of stimuli (*28*). In the contextual fear conditioning test, the initial acquisition of conditioned fear, which was measured by the percentage time freezing across successive presentations of mild electric foot shocks on day 1 of the test, was similar between PBS and CDS mice (Fig. 2C). Likewise, the two groups did not differ with regard to the expression of conditioned fear toward the context, which was assessed 24 hours after conditioning (Fig. 2C). Compared to PBS controls, however, CDS-treated mice displayed a deficit in the extinction of contextual fear memory, which was assessed by comparing the relative amount of conditioned freezing during successive days of context exposures relative to baseline freezing measured 24 hours after conditioning (Fig. 2C). Together, these data demonstrate that mice with a transient prefrontal microglia depletion in adolescence develop PFC-related cognitive deficits in adulthood, including impairments in social recognition memory, temporal order memory, and extinction of contextual fear memory. These deficits occurred without alterations in basal locomotor activity or indices of innate anxiety-like behavior, as analyzed by open-field and light-dark box tests (fig. S9).

To examine whether the stereotaxic surgery per se may have confounded the identified effects of CDS-induced prefrontal microglia depletion on cognitive development (Fig. 2), we compared the performance of mice receiving no stereotaxic injection (sham control mice) and mice receiving a bilateral stereotaxic injection of PBS in adolescence using the same battery of behavioral and cognitive tests in adulthood. These additional analyses revealed no differences between sham-treated and PBS-injected mice in terms of basal locomotor activity or indices of innate anxiety-like behavior, as analyzed by open-field (fig. S10A) and light-dark box (fig. S10B) tests. Likewise, sham-treated and PBS-injected mice did not differ in the tests assessing social approach behavior and social recognition memory (fig. S10C), temporal order memory (fig. S10D), or contextual fear conditioning and extinction (fig. S10E). These data show that the selected stereotaxic method did not induce any notable effects on behavioral and cognitive development, suggesting that the CDS-induced impairments in social recognition memory, temporal order memory, and extinction of contextual fear memory represent genuine long-term effects of prefrontal microglia depletion in adolescence.

Adult synaptic deficits after transient prefrontal microglia deficiency in adolescence

In keeping with the emerging role of microglia in synaptic refinement (*13*–*17*), we examined whether transient prefrontal microglia depletion in adolescence alters synaptic development and functions. First, we used Ingenuity Pathway Analysis (IPA) for functional network prediction of genes that were found to be differentially expressed in the PFC at the peak of CDS-induced microglia depletion, i.e., at 5 dpi in adolescence (Fig. 1). Consistent with the decrease in microglial cell density (Fig. 1, A and B), IPA identified the

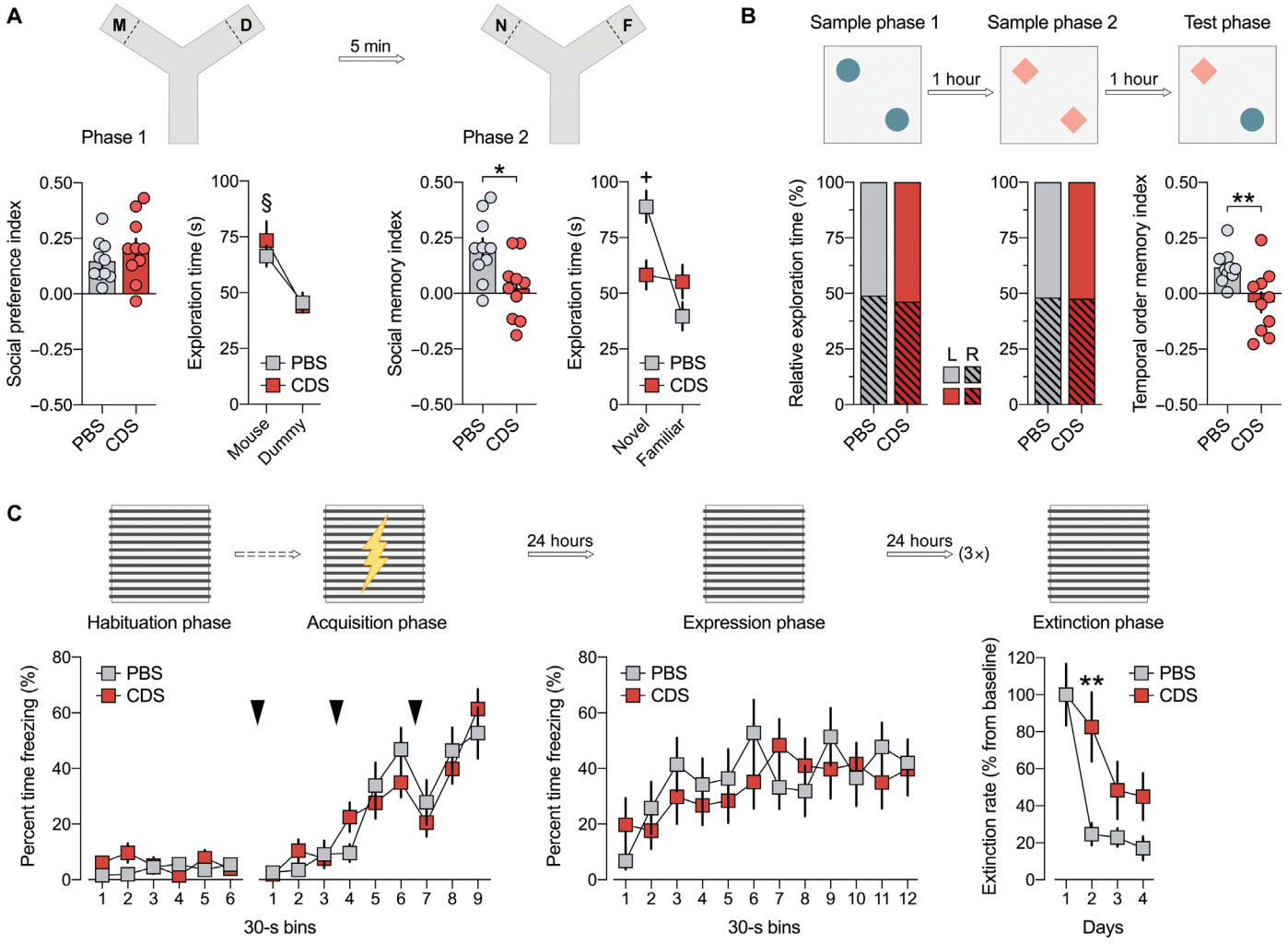

Fig. 2. Prefrontal microglia deficiency in adolescence disrupts adult cognitive functions. (**A**) Phase 1 (D, dummy object; M, unfamiliar mouse) and phase 2 (F, familiar mouse; N, novel mouse) of the social interaction test. The bar plots show the social preference index (phase 1) and social memory index (phase 2), whereas the line plots depict absolute exploration times in either phase. $^{§}P < 0.001$ [overall main effect of object: $F_{(1,18)} = 20.7$]; $^{*}P < 0.05$ [$t_{(18)} = 2.84$]; $^{+}P < 0.01$ [main effect of object in PBS mice: $F_{(1,9)} = 16.7$]. (**B**) The percentage plots depict the percentage amount of time exploring the left (L) or right (R) object in sample phases 1 and 2 of the temporal order memory test. The bar plot shows the temporal order memory index during the test phase. $^{**}P < 0.01$ [$t_{(18)} = 2.98$]. (**C**) Percent time freezing during the habituation, acquisition, and expression phases (left and middle line plots) and extinction rate (% change from freezing levels measured during the expression phase; right line plot) during the contextual fear test. The arrows indicate the presentation of foot shock. $^{**}P < 0.01$, based on post hoc tests following ANOVA [treatment × days interaction: $F_{(3,54)} = 2.9$, $P < 0.05$]. $N = 10$ mice in each group and test.

functional network "phagocytosis" to be dysregulated in CDS mice during this acute phase of adolescent microglia depletion (fig. S11). CDS mice also showed altered expression of genes annotating with the functional networks "axonal remodeling," "neurite remodeling," and "dendritic spine morphogenesis" (fig. S12) at 5 dpi, suggesting that acute deficiency of microglia in the adolescent PFC affects transcriptional programs pertaining to the remodeling of neuronal circuities. Intriguingly, a dysregulation of the functional networks "extracellular matrix organization and functions," "abnormal morphology of nervous system," "abnormal morphology of neurons," and "remodeling of neurites" persisted into adulthood after CDS treatment in adolescence (fig. S13), indicating that prefrontal microglia deficiency in adolescence may induce persistent changes in neuronal circuitries and synaptic structures.

To test this hypothesis, we first explored whether CDS-induced microglia depletion in the adolescent PFC alters the extent to which microglia engulf synaptic elements. To this end, we conducted immunohistochemical colocalization studies using the microglial marker, Iba1, and the presynaptic marker, Bassoon. We quantified the number of Bassoon^{+} synaptic puncta colocalizing with surface-rendered microglia (Fig. 3A). On the basis of the transcriptomic alterations aligning with phagocytosis (fig. S11), we expected the number of Bassoon^{+} synaptic puncta colocalizing with microglia to be decreased in CDS-injected mice relative to PBS controls. Consistent with our expectation, the number of Bassoon^{+} synaptic puncta was decreased in prefrontal microglia of CDS-injected mice at 10 dpi (Fig. 3B). At 20 dpi, however, CDS-injected mice displayed a significant increase in synaptic puncta colocalizing with microglia, whereas

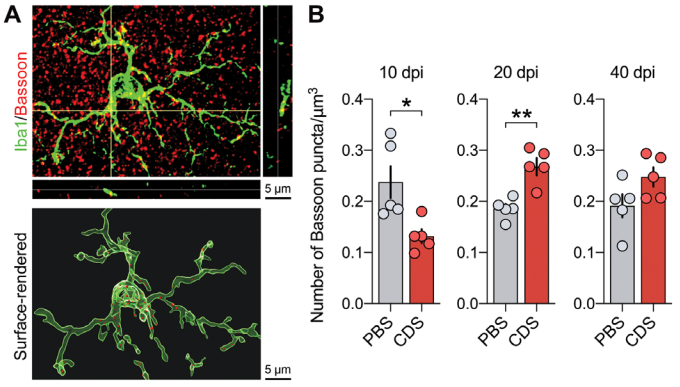

Fig. 3. Prefrontal microglia deficiency in adolescence leads to dynamic changes in microglial uptake of synaptic particles. (**A**) The photomicrograph shows a representative Z-stack image of a double-IF stain using Iba1 (green) as microglial marker and Bassoon (red) as presynaptic marker before (top) and after (bottom) surface rendering and reconstruction with Imaris image analysis software. Bassoon$^+$ presynaptic puncta colocalizing with Iba1$^+$ microglia appear in yellow in the unprocessed IF stain, whereas Bassoon$^+$ presynaptic puncta residing within microglia appear as red dots in the reconstructed image. (**B**) Quantification of Bassoon$^+$ presynaptic puncta residing within microglia at different days after injection. Note that the number of Bassoon$^+$ synaptic puncta was decreased in prefrontal microglia of CDS-injected mice at 10 dpi [$^*P < 0.05$, $t_{(8)} = 2.72$], whereas they were increased in CDS mice at 20 dpi [$^{**}P < 0.01$, $t_{(8)} = 4.28$]. There were no significant group differences at 40 dpi. All data are means ± SEM with individual values overlaid; $N = 5$ mice per group and dpi.

there were no significant group differences at 40 dpi (Fig. 3B). Hence, the data demonstrate dynamic changes in microglia-mediated synaptic engulfment after transient microglia deficiency in the adolescent PFC. While there was an initial decrease in synaptic engulfment by microglia shortly after the peak of their depletion, this decrease was followed by a phase of increased uptake of synaptic particles into prefrontal microglia.

On the basis of these findings, we investigated whether transient microglia depletion in adolescence is sufficient to cause lasting impairments in neuronal circuitries and synapses in the adult brain. We first compared the dendritic complexity of pyramidal neurons in the PFC of adult mice that were injected with CDS or PBS in adolescence. Sholl analysis of biocytin-labeled pyramidal neurons revealed that CDS mice displayed a reduction in the number of intersections at 60- to 80-µm distance from the soma center (Fig. 4A), demonstrating reduced complexity of dendritic arbors in close proximity of the cell soma. We then estimated the density of excitatory and inhibitory synapses in the adult PFC of PBS and CDS mice by analyzing the colocalization of presynaptic and postsynaptic markers. For excitatory synapses, we used the presynaptic marker vesicular glutamate transporter 1 (VGLUT1) and the postsynaptic marker postsynaptic density protein 95 (PSD-95) (*30*), whereas vesicular γ-aminobutyric acid (GABA) transporter (VGAT) and Gephyrin (*31*, *32*) were used as inhibitory presynaptic and postsynaptic markers, respectively. CDS treatment in adolescence similarly decreased the density of VGLUT1$^+$/PSD-95$^+$ colocalizing (Fig. 4B) and VGAT$^+$/Gephyrin$^+$ colocalizing synapses (Fig. 4C) in the adult PFC, indicating that transient prefrontal microglia depletion exerts lasting effects on the density of both excitatory and inhibitory synapses. These effects were further associated with a selective reduction of mushroom-shaped spines along the dendrites of prefrontal pyramidal neurons in adult mice that were subjected to adolescent CDS treatment (Fig. 4D), showing that the synaptic sequela of transient prefrontal microglia deficiency involves a specific pattern of dendritic spine pathology in the adult PFC.

To further explore whether these structural synaptic deficits are accompanied by functional changes in prefrontal neurons, we conducted whole-cell voltage clamp recordings of layer 2/3 pyramidal cells residing in the adult PFC of mice treated with PBS or CDS in adolescence. Passive biophysical properties (resting membrane potential and input resistance and capacitance) and action potential (AP)–related properties (AP firing threshold and frequency and AP half-width) of these cells were not different between PBS and CDS groups (fig. S14), indicating that the basic electrophysiological properties of prefrontal pyramidal cells were unaffected by the temporary prefrontal microglia depletion in adolescence. Likewise, the frequency and peak amplitude of spontaneous excitatory postsynaptic currents (sEPSCs) remained unaffected by adolescent CDS treatment (Fig. 5A). Compared to PBS controls, however, CDS mice displayed an increase in the frequency of spontaneous inhibitory postsynaptic currents (sIPSCs; Fig. 5B) and increased gene expression and protein levels of the alpha-1 subunit of the inhibitory GABA type A ($GABA_A$) receptor (Gabra1; fig. S15). There were no differences between CDS and PBS mice with regard to other alpha subunits of the $GABA_A$ receptor (fig. S15).

Relationship between cognitive and subregion-specific synaptic deficits after adolescent microglia deficiency

We also sought to identify possible relationships between cognitive and synaptic deficits in adult mice that were exposed to transient prefrontal microglia depletion in adolescence. To this end, we repeated selected cognitive (temporal order memory) and synaptic (density of VGLUT1$^+$/PSD-95$^+$ excitatory synapses and density of VGAT$^+$/Gephyrin$^+$ synapses) analyses in an independent cohort of adult mice that were subjected to intra-PFC CDS or PBS injections at 6 weeks of age (fig. S1) and determined possible correlations between these measures. Since distinct subregions of the PFC may contribute differentially to cognitive functions such as temporal order memory (*33*, *34*), these correlative analyses were conducted taking into account the IL, PL, and AC subregions of the PFC.

Consistent with our previous findings (Fig. 2B), we confirmed the presence of a temporal order memory deficit in adult mice that were subjected to transient prefrontal microglia depletion in adolescence (fig. S16A). The subsequent quantification of VGLUT1$^+$/PSD-95$^+$ puncta in distinct subregions of the PFC showed that microglia depletion in adolescence led to a selective reduction in the density of excitatory synapses in the AC subregion of the adult PFC (fig. S16B), whereas it decreased the density of VGAT$^+$/Gephyrin$^+$ inhibitory synapses in both PL and AC (fig. S16C). The adolescent CDS treatment did not alter the density of excitatory or inhibitory synapses in the IL subregion of the adult PFC (fig. S16, B and C). Pearson product-moment correlations identified positive correlations between the temporal order memory index and the density of excitatory (VGLUT1$^+$/PSD-95$^+$) in the AC and between this cognitive measure and the density of inhibitory (VGAT$^+$/Gephyrin$^+$) synapses in the AC and PL subregions (fig. S17). Subsequent group-wise analyses confirmed these positive correlations, although statistical significance was only obtained for the associations between the temporal order memory index and density of excitatory (VGLUT1$^+$/PSD-95$^+$) or inhibitory (VGAT$^+$/Gephyrin$^+$) synapses in the AC

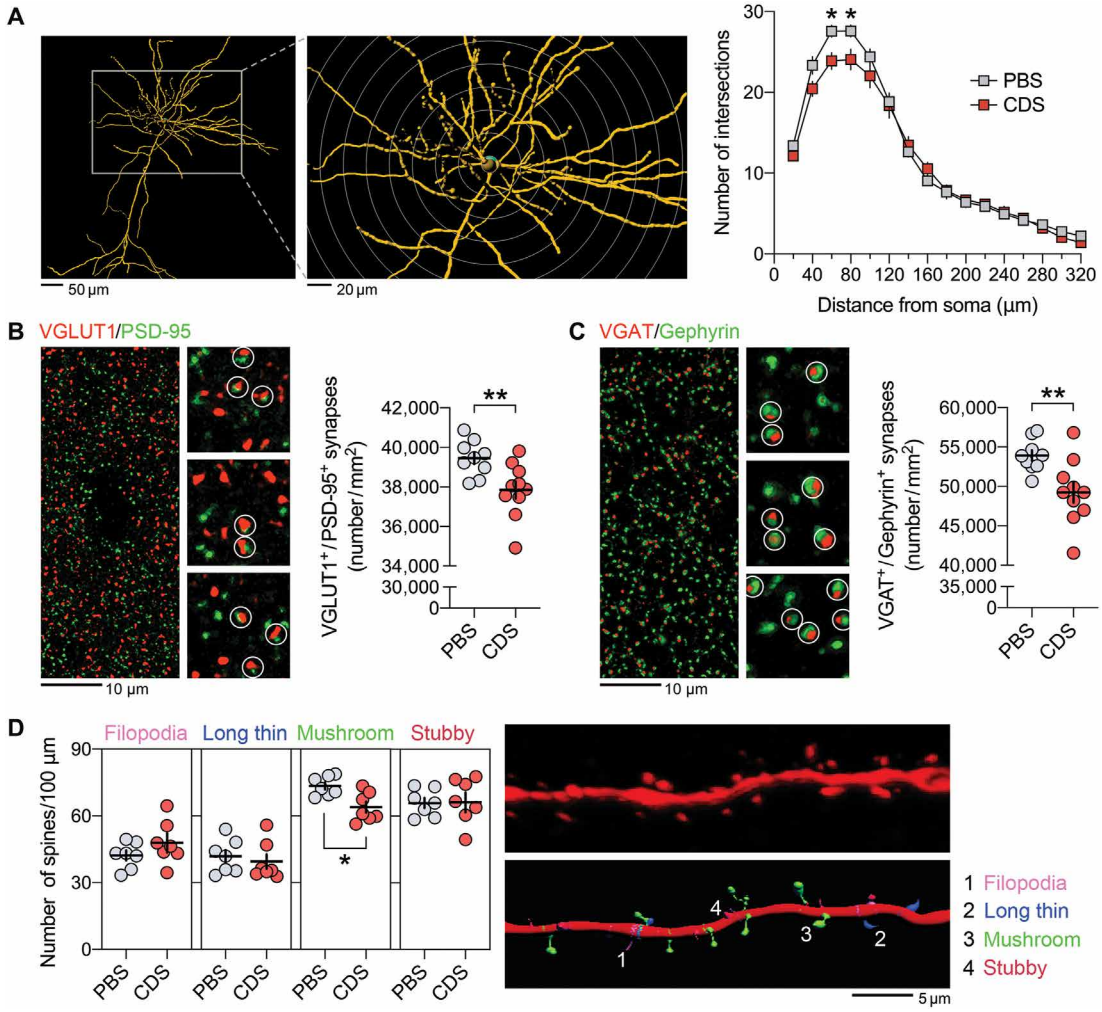

Fig. 4. Prefrontal microglia deficiency in adolescence induces structural synaptic changes in pyramidal neurons of the adult PFC. (**A**) Representative IF stain of a biocytin-filled pyramidal neuron reconstructed with Imaris image analysis software (left), with digitally applied concentric spheres (20-µm spacing) from the soma center (right). The line plot depicts the number of dendritic intersections against the radial distance from soma. $^{*}P < 0.05$, based on post hoc tests following ANOVA [treatment × distance interaction: $F_{(15,180)} = 2.7$, $P < 0.01$]; $N = 7$ mice per group. (**B**) Representative double-IF stain using VGLUT1 (red) as presynaptic and PSD-95 (green) as postsynaptic markers of excitatory neurons. VGLUT1^{+}/PSD-95^{+} colocalizing synapses are highlighted by white circles in magnified sections. The scatterplot shows the density (numbers per square millimeter) of VGLUT1^{+}/PSD-95^{+} synapses in the medial PFC of PBS ($N = 9$) and CDS ($N = 10$) mice. $^{**}P < 0.01$, $t_{(17)} = 2.97$. (**C**) Representative double-IF stain using VGAT (red) as presynaptic and Gephyrin (green) as postsynaptic markers of inhibitory neurons. VGAT^{+}/Gephyrin^{+} colocalizing synapses are highlighted by white circles in magnified sections. The scatterplot shows the density (numbers per square millimeter) of VGAT^{+}/Gephyrin^{+} synapses in the PFC of PBS ($N = 9$) and CDS ($N = 10$) mice. $^{**}P < 0.01$, $t_{(17)} = 2.88$. (**D**) The photomicrograph shows a representative IF stain of a biocytin-filled pyramidal dendritic section before (top) and after (bottom) surface rendering with Imaris. Different spine classes (1, filopodia; 2, long thin; 3, mushroom; and 4, stubby spines) are highlighted in different colors in the surface-rendered image. The scatterplots show the number of different spines. $^{*}P < 0.05$, $t_{(12)} = 3.22$; $N = 7$ mice per group.

subregion of CDS mice (fig. S16D). Together, these results show that transient prefrontal microglia depletion in adolescence had a more extensive impact on dorsal than on ventral subregions of the PFC in terms of synaptic densities. Moreover, our data suggest that synaptic deficits in the AC subregion of the PFC may be key in mediating adult cognitive impairments emerging after transient prefrontal microglia depletion.

Windows of vulnerability for cognitive and synaptic sequelae after microglia deficiency

The adult emergence of cognitive and synaptic deficits induced by transient prefrontal microglia depletion in adolescence likely stemmed from an interference with maturational processes occurring in the PFC from adolescent to adult stages. To further explore whether adolescence is a window of increased vulnerability for cognitive and synaptic sequelae after transient microglia deficiency, we applied the same microglia-depleting manipulation to adult mice (12 weeks of age; fig. S18) and examined possible effects on behavior and cognition. Consistent with the effects induced by adolescent CDS treatment (Fig. 1), intra-PFC injection of CDS in adult mice caused a 70 to 80% decrease in prefrontal microglia density (fig. S19A). Similar to when CDS was applied to adolescent mice (Fig. 1), the CDS-induced microglia depletion in adulthood was transient and was not associated with changes in the prefrontal density of astrocytes

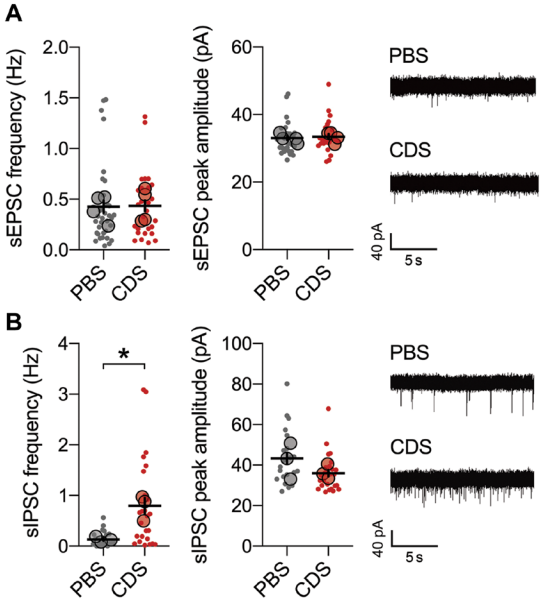

Fig. 5. Electrophysiological properties of pyramidal neurons in the adult PFC after transient prefrontal microglia depletion in adolescence. (**A**) sEPSC frequency and peak amplitude of pyramidal neurons in the adult PFC of PBS and CDS mice. Dots represent individual cells ($n = 35$ for PBS and $n = 27$ for CDS; $N = 4$ mice per group), whereas filled circles reflect cell averages per animal. The picture shows representative sEPSC traces for PBS and CDS mice. (**B**) sIPSC frequency and peak amplitude of pyramidal neurons in the adult PFC of PBS and CDS mice. Dots represent individual cells ($n = 26$ cells from $N = 3$ mice per group), whereas filled circles reflect cell averages per animal. *$P < 0.05$, $t_{(4)} = 4.35$, with animals as experimental unit. The picture shows representative sIPSC traces for PBS and CDS mice.

(fig. S19B) or neurons (fig. S19C). Despite the efficacy of the adult CDS treatment to deplete microglia from the adult PFC, this manipulation did not alter behavioral or cognitive functions (fig. S20) or electrophysiological parameters (fig. S21) after prefrontal microglia were repopulated. Furthermore, we did not observe any behavioral or cognitive changes when adult mice were tested during the time of ongoing microglia depletion in the PFC (fig. S22), indicating that adult prefrontal microglia have little direct impact on behavioral and cognitive functions, at least when considering the behavioral and cognitive domains investigated here.

To further explore possible windows of vulnerability for cognitive and synaptic sequelae after transient prefrontal microglia deficiency, we implemented the CDS-based microglia depletion model to 4-week-old mice with the aim to induce a transient depletion of prefrontal microglia in preadolescence (fig. S23). Consistent with the effects induced by adolescent CDS treatment (Fig. 1), intra-PFC injection of CDS in preadolescent mice caused a marked but transient decrease in the density of prefrontal microglia, which peaked at 5 dpi but was fully restored as of 10 dpi (fig. S24A). Preadolescent CDS treatment did not change the density of prefrontal neurons (fig. S24B) or astrocytes (fig. S24C) during the acute and post-acute phases of microglia depletion. Mice receiving a bilateral intra-PFC injection of CDS in preadolescence developed behavioral and cognitive changes in adulthood, which were partially distinct from those induced by transient prefrontal microglia depletion in adolescence. More specifically, adult mice subjected to the CDS treatment in preadolescence displayed a higher social preference index in the social interaction test (Fig. 6A), while they did not differ from PBS controls in terms of social recognition memory (Fig. 6A) or temporal order memory (Fig. 6B). Similar to mice receiving CDS in adolescence (Fig. 2C), however, mice subjected to the microglia-depleting manipulation in preadolescence developed a deficit in the extinction of contextual fear memory at adult age (Fig. 6C), which was unrelated to possible changes in innate anxiety-like behavior (fig. S25). Together, our data demonstrate that the adult PFC, unlike the maturing PFC, is resilient to transient microglia deficiency in terms of possible behavioral and cognitive maladaptations. Moreover, our findings suggest that the precise timing of prefrontal microglia depletion during postnatal development critically determines the specificity of adult brain dysfunctions.

Consistent with this notion, we found that prefrontal microglia depletion in preadolescence produces a spectrum of adult synaptic abnormalities that substantially differed from the long-term synaptic changes induced by prefrontal microglia depletion in adolescence. Unlike CDS treatment in adolescence (Fig. 4A), the same manipulation did not alter the dendritic complexity of pyramidal neurons in the adult PFC when it was implemented in preadolescence (Fig. 7A). Moreover, in contrast to prefrontal microglia depletion in adolescence (Fig. 4, B and C), preadolescent microglia depletion failed to induce a global decrease in excitatory ($VGLUT1^+/PSD\text{-}95^+$) or inhibitory ($VGAT^+/Gephyrin^+$) synaptic densities in the adult PFC (Fig. 7, C and D). CDS treatment in preadolescence did, however, lead to a modest but significant decrease in the number of long-thin spines in the adult PFC, as evaluated by Imaris-guided quantification of surface-rendered pyramidal dendritic sections (Fig. 7B). Concomitant to the differential effects of the preadolescent or adolescent manipulations on synaptic structures, the precise timing of prefrontal microglia depletion also influenced the specificity of functional synaptic alterations. While CDS treatment in adolescence led to an increase in the frequency of sIPSCs in adult prefrontal neurons (fig. S26A), CDS treatment during the earlier postnatal stage reduced the peak amplitude of sIPSCs while sparing sIPSC frequency (fig. S26B). CDS treatment in preadolescence did not alter the frequency or peak amplitude of sEPSCs in adult prefrontal neurons (fig. S26, A and B), nor did it change basic electrophysiological properties of prefrontal pyramidal cells (fig. S26, C and D).

DISCUSSION

The protracted maturation of the PFC is necessary for acquiring mature cognitive abilities in adulthood (*1*–*5*). Our data now implicate microglia as a regulator of this maturational process and show that a cell-specific and temporary deficiency of prefrontal microglia during restricted stages of adolescence is sufficient to cause lasting synaptic and cognitive impairments in adulthood. It is likely that prefrontal microglia influence cognitive development by means of refining dendritic and synaptic structures (*18*). In support of this notion, we identified dynamic changes in microglia-mediated synaptic engulfment after transient microglia deficiency in the adolescent PFC. While there was an initial decrease in the uptake of synaptic particles into prefrontal microglia shortly after the peak of their depletion (i.e., at 10 dpi), this decrease was followed by a phase of increased synaptic engulfment by prefrontal microglia. The latter may provide a parsimonious explanation for the seemingly paradoxical effects of transient microglia deficiency on synaptic densities in the adult PFC. Rather than causing an increase, transient

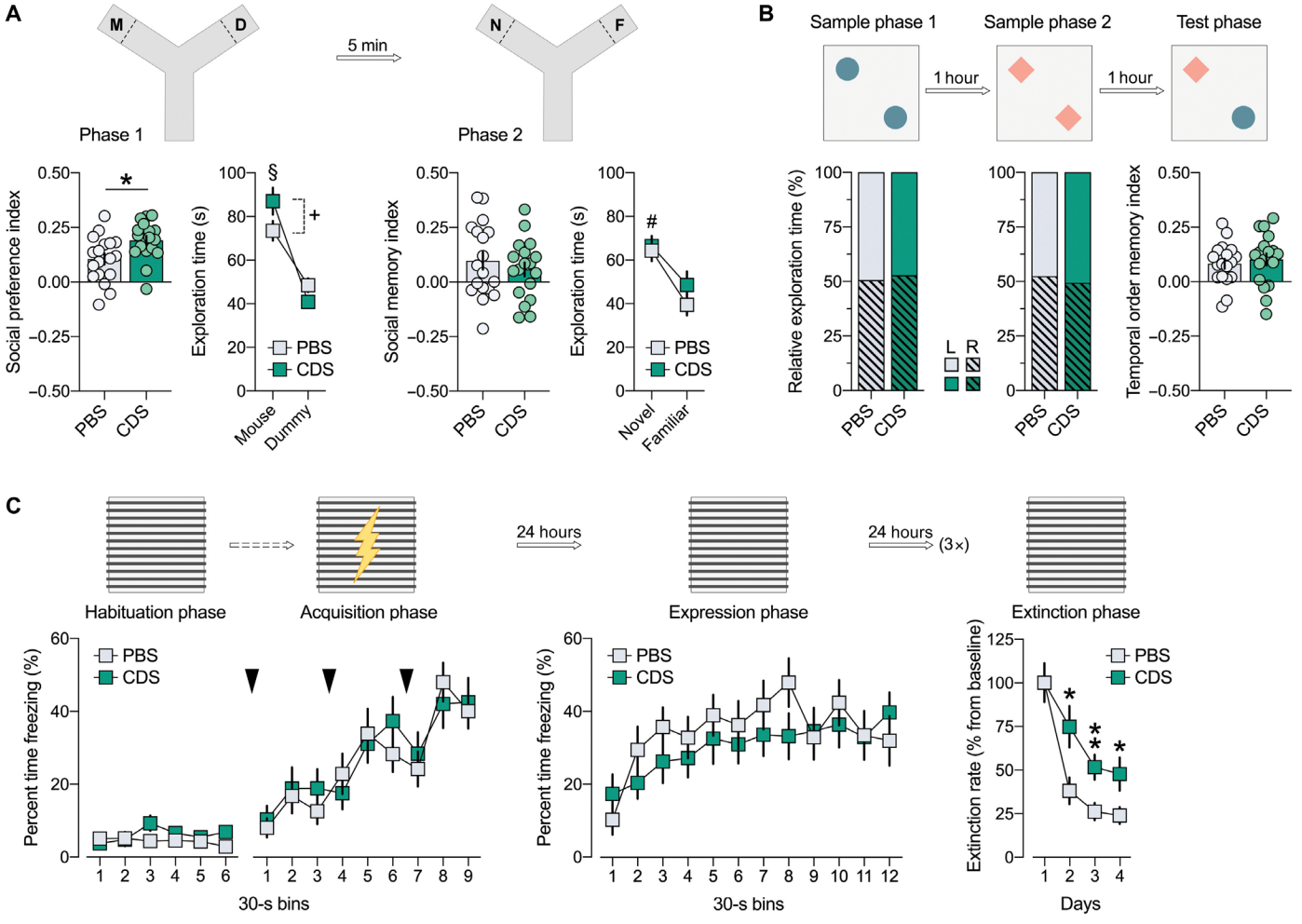

Fig. 6. Prefrontal microglia deficiency in preadolescence causes selective behavioral and cognitive changes in adulthood. (**A**) Phase 1 (D, dummy object; M, unfamiliar mouse) and phase 2 (F, familiar mouse; N, novel mouse) of the social interaction test. The bar plots show the social preference index in phase 1 (values > 0 represent a preference toward M) and social memory index in phase 2 (values > 0 represent a preference toward N), whereas the line plots depict absolute exploration times in either phase. $^{*}P < 0.05$ [$t_{(34)} = 2.6$]; §$P < 0.001$ [$F_{(1,34)} = 46.7$], reflecting the overall main effect of object in phase 1; $^{+}P < 0.05$, reflecting the difference between PBS and CDS mice in terms of the time spent exploring the live mouse, based on post hoc tests following ANOVA [treatment × object interaction: $F_{(1,34)} = 3.8$, $P < 0.05$]; $^{\#}P < 0.01$, reflecting the overall main effect of object in phase 2 [$F_{(1,34)} = 8.4$]. (**B**) The percentage bar plots depict the relative amount of time (%) exploring the left (L) or right (R) object in sample phases 1 and 2 of the temporal order memory test. The bar plot shows the temporal order memory index during the test phase (values > 0 represent a preference toward the temporally more remote object presented in sample phase 1). (**C**) Percent time freezing during the habituation, acquisition, and expression phases (left and middle line plots) and extinction rate (% change from freezing levels measured during the expression phase; right line plot) during the contextual fear test. The arrows indicate the presentation of foot shock. $^{*}P < 0.05$ and $^{**}P < 0.01$, based on post hoc tests following repeated-measures ANOVA [treatment × days interaction: $F_{(3,102)} = 3.2$, $P < 0.05$]. All data are means ± SEM with individual values overlaid; $N = 18$ male mice in each group and test.

microglia deficiency in adolescence eventually led to an overall decrease in synaptic densities at adult age. We also revealed a notable relationship between the degree of synaptic and cognitive deficits emerging in mice that were subjected to prefrontal microglia deficiency in adolescence. Consistent with previous lesion or imaging studies implicating dorsal PFC subregions in temporal behavioral sequencing and temporal ordering of events (*35*–*37*), we found that prefrontal synaptic densities in the AC were positively correlated with the capacity of CDS-treated mice to discriminate the relative recency of stimuli. Together, we provide converging evidence suggesting that altered synaptic refinement links prefrontal microglia deficiency in adolescence with the emergence of PFC-associated cognitive impairments in adulthood.

By showing that the cognitive effects of intra-PFC CDS treatment were markedly influenced by the precise postnatal timing, our study also identified critical windows of vulnerability for cognitive sequelae after transient prefrontal microglia deficiency. While CDS-based prefrontal microglia depletion in adult mice failed to induce short- or long-term effects on behavior and cognition, the same manipulation caused lasting cognitive dysfunctions when implemented in preadolescence or adolescence, with notable differences existing between the two latter time windows as well. For example, preadolescent CDS exposure failed to alter social recognition memory and temporal order memory, both of which were disrupted by adolescent CDS treatment only. These timing-dependent effects were unlikely to be the result of a varying degree of microglia depletion, as

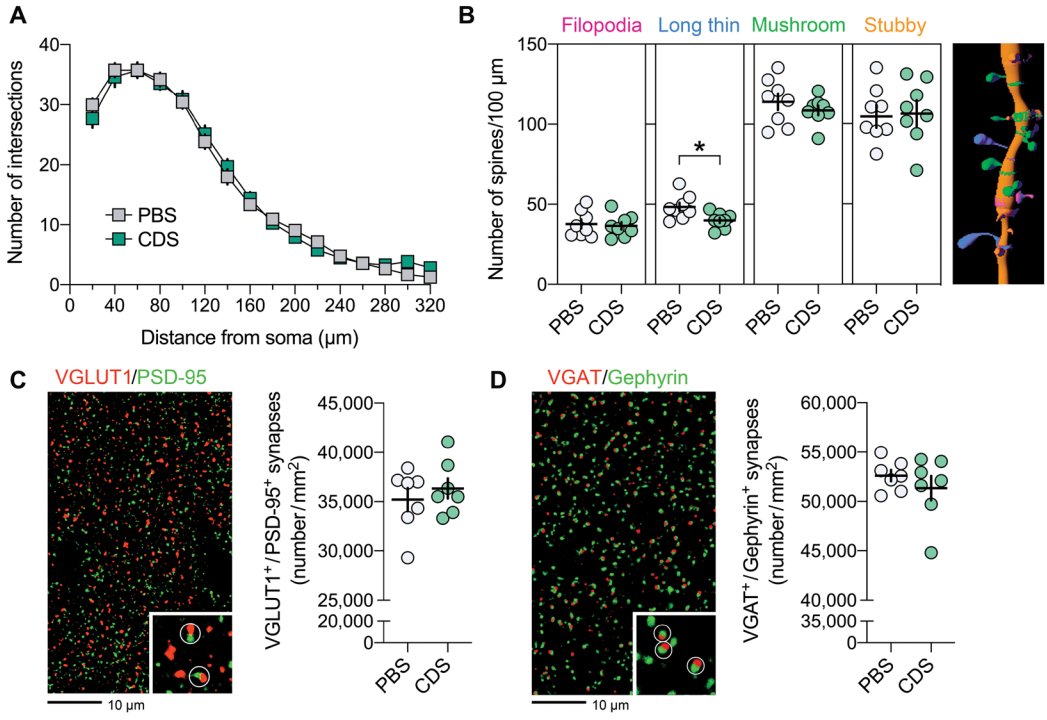

Fig. 7. Restricted structural synaptic changes in pyramidal neurons of the adult PFC after transient prefrontal microglia deficiency in preadolescence. (**A**) The line plot depicts the number of dendritic intersections against the radial distance from soma (20-µm spacing from the soma center), as analyzed by Sholl analysis of biocytin-filled prefrontal neurons reconstructed with Imaris image analysis software. $N = 8$ per group. (**B**) Number of different spines (filopodia, long-thin, mushroom, and stubby spines), as analyzed by quantification of surface-rendered spines on biocytin-filled pyramidal dendritic sections. Different spine classes are highlighted in different colors, as shown on the representative IF stain of a biocytin-filled pyramidal dendritic section after surface rendering with Imaris. $^*P < 0.05$, $t_{(14)} = 2.66$; $N = 8$ per group. (**C**) Representative double-IF stain using VGLUT1 (red) as presynaptic and PSD-95 (green) as postsynaptic markers of excitatory neurons. VGLUT1$^+$/PSD-95$^+$ colocalizing synapses are highlighted by white circles in the magnified section. The scatterplot shows the density (numbers per square millimeter) of VGLUT1$^+$/PSD-95$^+$ synapses in the medial PFC of PBS and CDS mice. $N = 7$ per group. (**D**) Representative double-IF stain using VGAT (red) as presynaptic and Gephyrin (green) as postsynaptic markers of inhibitory neurons. VGAT$^+$/Gephyrin$^+$ colocalizing synapses are highlighted by white circles in the magnified section. The scatterplot shows the density (numbers per square millimeter) of VGAT$^+$/Gephyrin$^+$ synapses in the PFC of PBS and CDS mice $N = 7$ per group.

intra-PFC injections of CDS in preadolescence or adolescence caused a highly comparable degree of microglia depletion (70 to 80% reduction at the peak of the depletion under both conditions). Rather, the differential effects of preadolescent or adolescent CDS treatment may be accounted for by a timing-dependent disruption of ongoing maturational processes, which partly differ between preadolescent and adolescent stages of prefrontal maturation (*3*–*5*). Establishing and strengthening the excitatory/inhibitory balance, which is achieved through the remodeling of the glutamatergic and GABAergic systems, is one of the key processes that characterize the adolescent maturation of the PFC (*4*). The GABAergic system undergoes major remodeling steps during adolescence, whereas the glutamatergic system itself is remodeled only marginally. Two illustrative examples for the notable GABAergic changes occurring during adolescent PFC maturation involve local GABAergic interneurons expressing parvalbumin (PV) or calretinin (CR), which show opposite maturational trajectories (*3*, *38*). Upon reaching adolescence, fast-spiking interneurons up-regulate PV expression, whereas CR expression decreases sharply during this time (*3*, *38*). Upon reaching adolescence, prefrontal pyramidal neurons also start displaying enhanced sIPSC frequencies (*39*), which, in turn, seems to be related to a concomitant increase in Gabra1 expression (*3*). Because of these maturational trajectories, the consequences of disrupting prefrontal GABAergic remodeling are likely to be different when the disrupting event takes place in preadolescence or adolescence. Consistent with this notion, we found that prefrontal microglia depletion in adolescence led to increased sIPSC frequencies and higher Gabra1 expression in the adult PFC, whereas the same manipulation failed to do so when implemented in preadolescence.

However, some effects of transient prefrontal microglia depletion similarly emerged regardless of whether the depletion coincided with preadolescence or adolescence. Such timing-independent effects were, for example, observed in contextual fear extinction, which was equally impaired in adult mice that had been treated with CDS at 4 or 6 weeks of age. The basic neural circuitries mediating fear extinction develop already at juvenile stages of life (*40*–*42*), with fine-tuning and refinement occurring thereafter throughout periadolescence (*43*, *44*). Thus, the microglia-depleting manipulations in 4- or 6-week-old mice targeted preexisting, basic neuronal circuitries of fear extinction, possibly leading to a mal-refinement of these circuitries across subsequent brain maturation in both cases. If confirmed by future investigations, then the early development and subsequent maturation of fear extinction circuitries may indeed offer an explanation as to why transient prefrontal microglia depletion in preadolescence or adolescence induced similar effects in this cognitive domain.

While several genetic and pharmacological models of microglia depletion exist (*19*–*24*), the model presented here is unique in that it allows for a selective manipulation of microglia in a brain region–specific and temporally restricted manner without inducing nonspecific effects on peripheral immune cells. This degree of specificity is not reached by other models, be it because they lack brain region specificity (*19*–*23*) and/or are associated with a suppression or depletion of peripheral immune cells, including monocytes and macrophages (*45*). However, one possible limitation of the model presented here is that it requires stereotaxic surgery to induce transient microglia depletion, and thus, it causes local tissue damage at the site of the intracerebral injection. To control for possible confounds resulting from local tissue damage, we included additional cohorts of sham control mice, which underwent the same experimental manipulations as PBS controls (including anesthesia, fixation in the stereotaxic frame, and longitudinal skin incision), except that they did not receive any intracerebral injection. We found that sham controls did not differ from PBS controls with regard to the densities in terms of microglia, neurons, or astrocytes or in terms of microglial gene expression after microglia repopulation. Moreover, sham and PBS control mice did not differ in terms of their behavioral and cognitive performance throughout all tests of interest. On the basis of these findings, we conclude that the local tissue damage caused by the intracerebral injection did not confound the identified effects of CDS-induced microglia depletion, implying furthermore that the synaptic and cognitive changes emerging after transient prefrontal microglia depletion cannot be accounted for by the stereotaxic injection itself.

We acknowledge a number of limitations in our study. First, because our study was based on investigations in male mice only, an extension to other species and female subjects is warranted to test the generalizability of our findings across species and sex. The latter appears particularly important in view of the known sex differences in microglia biology in health and disease (*46*). Second, while our data strongly implicate microglia in the structural and functional maturation of the PFC, the precise molecular mechanisms by which these cells regulate prefrontal maturation remain to be identified in future studies. Third, the identified associations between cognitive and subregion-specific synaptic deficits emerging after transient prefrontal microglia deficiency are based on correlative evidence only. Thus, additional studies are warranted to ascertain causal relationships between synaptic and cognitive measures in this model. Likewise, the precise relationships between structural and functional synaptic abnormalities await further exploration. For example, while our study revealed timing-dependent effects of transient microglia deficiency on synaptic densities and electrophysiological parameters in the PFC, the extent to which the identified synaptic deficits contribute or even mediate the observed alterations in sIPSC remains elusive.

Notwithstanding these limitations, our study identifies adolescence as a critical period during which prefrontal microglia act on cognitive development. The experimental model system described here offers unique opportunities to investigate the pathophysiological relevance of impaired microglial functions in neurodevelopmental disorders, especially those that involve structural and functional deficits in the PFC. While hypotheses surrounding an involvement of increased microglial activity in neurological and psychiatric disorders have rapidly gained momentum in recent years (*47*–*49*), our findings emphasize that the opposite pathology, namely, microglial deficiency, is likely to be etiologically relevant for some brain disorders as well, especially for those that have their typical onset in late adolescence or early adulthood (*50*).

MATERIALS AND METHODS

Animals

All experiments were performed using male C57BL6/N mice (Charles Rivers, Sulzfeld, Germany). We included animals of one sex (male) only, as our study was primarily designed to identify timing-dependent effects of transient prefrontal microglia depletion, which required the generation of multiple cohorts of animals. Hence, the inclusion of both sexes was not technically feasible in the current study. The animals were kept in groups (two to five animals per cage) in individually ventilated cages (Allentown Inc., Bussy-Saint-Georges, France) in a temperature- and humidity-controlled (21° ± 3°C, 50 ± 10%) specific pathogen–free holding room. They were kept under a reversed light-dark cycle (lights off: 9:00 a.m. to 9.00 p.m.) and had ad libitum access to standard rodent chow (Kliba 3336, Kaiseraugst, Switzerland) and water throughout the entire study. All experiments were previously approved by the Cantonal Veterinarian's Office of Zürich, Switzerland (license no. ZH-187/2017). All efforts were made to minimize the number of animals used and their suffering. The number of animals used in each experiment is specified in the legends of the main figures (Figs. 1 to 7) and supplementary figures (figs. S1 to S25).

Stereotaxic surgery

The stereotaxic surgery was performed using methods established and validated before (*51*, *52*). Anesthesia of the animals was induced by inhalation of 2 to 3% isoflurane (ZDG9623V, Baxter, Switzerland) in oxygen. After anesthesia induction, the heads of the animals were shaved, and vitamin A cream (Bausch & Lomb Swiss AG) was applied to the eyes to avoid dehydration. The animals were injected with the analgesic Temgesic [buprenorphine (0.1 mg/kg, s.c.), Reckitt Benckiser, Switzerland] and fixed into the stereotaxic frame (MTM-3, World Precision Instruments, USA) while kept under constant isoflurane/oxygen flow [1 to 3% isoflurane in oxygen (600 ml/min)]. All animals were kept on a temperature-controlled heating plate (ATC1000, World Precision Instruments, USA) during the entire surgical procedure to avoid anesthesia-induced hypothermia. A longitudinal incision of the skin was made to expose the skull. The skull was cleaned from connective tissue, and the bone, above the target area, was removed using a micro drill (OmniDrill35, World Precision Instruments, USA) with a rose burr (ø 0.3 mm). Intracerebral injections were performed using a NanoFil needle and syringe (NANOFIL, NF35BV, World Precision Instruments, USA) connected to an automated pump (UMP3T-1, World Precision Instruments, USA).

Mice assigned to transient prefrontal microglia depletion received a single, bilateral injection of CDS (50 mg/ml in PBS; catalog no. 233183, EMD Millipore Corp., USA) into the medial portion of the PFC, whereas control mice received a single, bilateral injection of PBS (catalog no. 14190144, Thermo Fisher Scientific, Switzerland). The solutions were injected at an infusion rate of 5 nl/s and a volume of 200 nl (4- and 6-week-old mice) or 300 nl (12-week-old mice). Bilateral injections were performed at defined stereotaxic coordinates of the PFC with reference to bregma. For preadolescent (4-week-old) mice, the following coordinates were used: anteroposterior

(A/P) = +1.75 mm, mediolateral (M/L) = ±0.3 mm, and dorsoventral (D/V) = −1.65 mm; for adolescent (6-week-old) mice, the following coordinates were used: A/P = +1.80 mm, M/L = ±0.3 mm, and D/V = −1.90 mm; and for adult (12-week-old) mice, the following coordinates were used: A/P = +2.0 mm, M/L = ±0.3 mm, and D/V = −2.0 mm. After insertion of the needle, a small drop of Histoacryl (B. Braun, Switzerland) was applied at the site of injection to avoid reflux of the injected substances. After injection of either PBS or CDS, the needle was kept in place for 5 min to avoid reflux of the substances before retracting it. For some experiments, an additional group of animals was fixed into the stereotaxic frame and had a longitudinal incision made but were otherwise left undisturbed. These mice served as additional sham controls. Incisions were sutured with a surgical thread (G0932078, B. Braun, Switzerland), and the animals were placed in a temperature-controlled chamber (Harvard Apparatus, USA) until full recovery from anesthesia. After the surgery, the animals were placed back in their home cage and closely monitored for three consecutive days after surgery.

Behavioral and cognitive testing

Behavioral and cognitive testing involved a battery of tests indexing basal locomotor activity and innate anxiety-like behavior (open-field test and light-dark box test), social approach behavior and recognition memory (social interaction test), temporal order memory for objects (temporal order memory test), and contextual fear conditioning and extinction (fear conditioning test). The tests for social approach behavior and recognition memory, temporal order memory, and contextual fear conditioning and extinction were selected because they critically involve PFC functions (*27*–*29*). Tests for basal locomotor activity and innate anxiety-like behavior were conducted to evaluate whether the anticipated changes in PFC-related cognitive functions after microglia depletion would be confounded by possible alterations in general exploratory activity or innate anxiety-like behavior. In each experimental series, the animals were tested repeatedly using the same order of testing [(i) open-field test, (ii) light-dark box test, (iii) social interaction test, (iv) temporal order memory test, and (v) fear conditioning test], with a resting phase of 3 to 4 days between individual tests. Testing was always conducted during the animals' active phase, that is, during the dark phase of the inverted light-dark cycle (between 10:00 a.m. and 8.00 p.m.). All tests were extensively validated previously and are routinely used in our laboratory (*53*–*56*).

Open-field test

A standard open-field exploration task served as the first test to assess spontaneous locomotor activity and innate anxiety-like behavior (*57*). The apparatus consisted of four identical open-field arenas [40 cm (length) by 40 cm (width) by 35 cm (height)] made of white polyvinyl chloride (OCB Systems Ltd., Hertfordshire, UK). It was positioned in a testing room with diffused lighting (~30 lux in the center of the arena). A digital camera was mounted above the arena, captured images at a rate of 5 Hz, and transmitted them to a PC running the EthoVision (Noldus Technology, Wageningen, The Netherlands) tracking system. The animals were recorded for 15 min before they were placed back into their home cage. For the purpose of data collection, the arena was conceptually partitioned into two areas: a center zone (measuring 10 cm by 10 cm) in the middle of the area and a peripheral zone occupying the remaining area. The measurements collected from this test included the total distance moved, the distance moved in the center zone, and the number of center zone visits.

Light-dark box test

A light-dark box test was used as the second test to measure innate anxiety-like behavior (*57*). The apparatus consisted of four identical multiconditioning boxes (Multi Conditioning System, TSE Systems, Bad Homburg, Germany), each containing a dark (1 lux) and a bright (100 lux) compartment. The two compartments were separated from each other by a dark plexiglass wall with an integrated, electrically controlled door. To start a trial, each mouse was placed in the dark compartment. After 5 s, the door automatically opened, allowing access to both the dark and bright compartments for 10 min. The measurements collected from this test included the distance moved and time spent in the light compartment.

Social approach and social recognition memory test

Social approach behavior and social recognition memory were measured using a social interaction test consisting of two phases (*54*, *55*). The apparatus was made of a modified Y-maze consisting of an opaque acrylic glass, which contained three identical arms [50 cm (length) by 9 cm (width)] surrounded by 10-cm-high Plexiglas walls. The three arms radiated from a central triangle (8 cm on each side) and were spaced 120° from each other. Two of the three arms contained rectangular wire grid cages [13 cm (length) by 8 cm (width) by 10 cm (height)], with metal bars horizontally and vertically spaced 9 mm apart. The third arm did not contain a metal wire cage and served as the start zone (see below). The apparatus was located in an experimental testing room under dim diffused lighting (~20 lux as measured in the individual arms).

Phase 1. This phase served as a test for social approach behavior. During this phase, one metal wire cage contained an unfamiliar C57BL6/N mouse ("live mouse"), whereas the other wire cage contained an inanimate object ("dummy object"). The latter was a black scrunchie made of velvet material. The allocation of the live mouse and "dummy" to the two wire cages was counterbalanced across experimental groups. To begin a trial, the test animal was introduced at the end of the start arm and was allowed to freely explore all three arms for 5 min. Behavioral observations were made by an experimenter who was blinded to the experimental conditions in the form of numerical codes. Social interaction was defined as a nose contact within a 2-cm interaction zone. For each test animal, a social preference index was calculated by the following formula: [(time spent with the mouse)/(time spent with the inanimate dummy object + time spent with the mouse)] − 0.5. The social preference index was used to compare the relative exploration time between the unfamiliar mouse and the inanimate dummy object, with values > 0 signifying a preference toward the unfamiliar mouse. In addition, the absolute times spent with the unfamiliar mouse and the inanimate dummy object were analyzed. On completion of phase 1, the animal was removed and kept in a holding cage for 5 min until the start of the next phase.

Phase 2. This phase served as a test for social recognition memory. During this phase, another unfamiliar C57BL6/N mouse, which is referred to as the "novel mouse," replaced the inanimate dummy object. The other cage contained the "familiar mouse" previously used in phase 1 (see above) of the test. The allocation of the novel mouse and familiar mouse to the two wire cages was counterbalanced across experimental groups. To start phase 2, the test animal was introduced at the end of the start arm and was allowed to freely explore all three arms for 5 min. Behavioral observations for social interaction were scored as described before. For each test animal, a social memory index was calculated by the following formula:

[(time spent with the novel mouse)/(time spent with the novel mouse + time spent with the familiar mouse)] − 0.5. The social memory index was used to compare the relative exploration time between the familiar and novel mice, with values > 0 signifying a preference toward the novel mouse. In addition, the absolute times spent with the familiar and novel mice were analyzed.

Temporal order memory test

A temporal order memory test for objects was used to measure the PFC-dependent capacity of animals to discriminate the relative recency of stimuli (*28*). The test apparatus consisted of an open field as described above, with minor modifications (see below). The test procedure consisted of four consecutive phases, which were each separated 60 min apart.

Habituation phase. To habituate the animals to the test apparatus, the animals were gently placed in the center of the open-field apparatus and allowed to freely explore the arena for 10 min. They were then removed from the apparatus and kept in a holding room for 60 min before the start of the next phase.

Sample phase 1. For this phase, a first pair of identical objects (blue aluminum hairspray bottles, 250 ml, 20 cm high) were placed in the open-field arena in opposing corners approximately 5 cm from the walls. To start a trial, the animals were gently placed into the center of the open field and were allowed to freely explore the objects for 10 min. They were then removed from the apparatus again and kept in a holding room for 60 min before the start of the next phase.

Sample phase 2. For this phase, a novel pair of identical objects (LEGO Duplo brick pile, 15 cm high) were placed in the open-field arena, thereby allocating them in the same position as the first pair of objects (see above). To start a trial, the animals were gently placed into the center of the open field again and were allowed to freely explore the novel pair of objects for 10 min. They were then removed from the apparatus once more and kept in a holding room for 60 min before the start of the actual test phase.

Test phase. In the test phase, the open field was equipped with one object used in sample phase 1 (temporally more remote object) and one object in sample phase 2 (temporally more recent object), with the corner allocation of the objects being counterbalanced across groups. To start the test trial, the animals were placed into the center of the open field and were allowed to freely explore either object for 10 min.

For each animal, a temporal order memory index was calculated by the following formula: [(time spent with phase 1 object)/(time spent with phase 1 object + time spent with phase 2 object)] − 0.5. The temporal order memory index was used to compare the animals' capacity to discriminate the relative recency of stimuli (*16*), with values > 0 signifying a capacity to discriminate between the temporally more remote object presented in sample phase 1 and the temporally more recent object presented in sample phase 2. In addition, the relative amount of time exploring the objects in sample phases 1 and 2 of the test was analyzed to measure object exploration per se and to explore possible side preferences while exploring the objects.

Contextual fear conditioning and extinction

Contextual fear conditioning and extinction were conducted using four identical multiconditioning chambers (Multi Conditioning System, TSE Systems, Bad Homburg, Germany), in which the animals were confined to a rectangular enclosure [30 cm (length) by 30 cm (width) by 36 cm (height)] made of black acrylic glass. The chambers were equivalently illuminated by a red house light (30 lux) and were equipped with a grid floor made of 29 stainless rods (4 mm in diameter and 10 mm apart; inter-rod center to inter-rod center), through which a scrambled electric shock could be delivered. Each chamber was surrounded by three infrared light–beam sensor systems, with the sensors spaced 14 mm apart, allowing movement detection in three dimensions. The contextual fear conditioning and extinction test followed protocols established before (*53*) and consisted of three phases, which were each separated 24 hours apart (see below). During all three phases, the red house light was on at all times. Conditioned fear was expressed as freezing behavior, which was quantified automatically by program-guided algorithms as the time of immobility per 30-s bins. The data collected during the three phases were analyzed separately.

Habituation and conditioning phase. The animals were placed in the designated test chamber and were allowed to freely explore the chamber for 3 min. This served to habituate the animals to the chamber. Conditioning commenced immediately at the end of the habituation period without the animals being removed from the chambers. For conditioning, the animals were exposed to three conditioning trials, whereby each conditioning trial began with the delivery of a 1-s foot-shock set at 0.3 mA and was followed by a 90-s rest period. After conditioning, the animals were removed from the chambers and were placed back in their home cages immediately after the last trial. The amount of percent time freezing during each post-shock period was divided into bins of 30 s and provided a measure of the contextual fear acquisition.

Fear expression phase. The fear expression phase took place 24 hours after conditioning when the animals were returned to the same chambers in the absence of any discrete stimulus other than the context. To assess conditioned fear toward to the context, percent time freezing was measured for a period of 6 min and expressed as a function of 30-s bins. The animals were then removed from the boxes and placed back to their home cages.

Fear extinction phase. Extinction of contextual fear memory was evaluated by daily exposing the animals to the same chambers in the absence of any discrete stimulus other than the context (*17*). This procedure was conducted on three consecutive days, during which the animals were exposed to the chamber for a total of 6 min on each day. To analyze extinction of contextual fear memory, the extinction rate was calculated for each animal by expressing the percent time freezing measured on each day of the fear extinction phase relative to the baseline percent time freezing measured during the fear expression phase 24 hours after conditioning.

Electrophysiology

Coronal slices (300 μm) of the PFC were prepared from adult C57BL6/N male mice treated with PBS or CDS in preadolescence, adolescence, or adulthood (see above). Slices were incubated for 1 hour at 34°C in sucrose-containing artificial cerebrospinal fluid (sucrose-ACSF: 85 mM NaCl, 75 mM sucrose, 2.5 mM KCl, 25 mM glucose, 1.25 mM sodium phosphate buffer, 4 mM $MgCl_2$, 0.5 mM $CaCl_2$, and 24 mM $NaHCO_3$) and then held at room temperature in the same solution until recording. Electrophysiological recordings were made at 37°C in ACSF (126 mM NaCl, 2.5 mM KCl, 10 mM glucose, 1.25 mM sodium phosphate buffer, 2 mM $MgCl_2$, 2 mM $CaCl_2$, and 26 mM $NaHCO_3$) containing (2*R*)-amino-5-phosphonovaleric acid (10 μM; catalog no. 79055-68-8, Tocris Bioscience) and 2,3-dioxo-6-nitro-7-sulfamoyl-benzo[*f*]quinoxaline (5 μM; catalog no. 118876-58-7, Tocris Bioscience) to record IPSCs, whereas ACSF containing hydrobromide/gabazine (10 μM; catalog no. 104104-50-9, Tocris

Bioscience) was used to record EPSCs. Slices were visualized in an upright microscope (BX-61WI, Olympus) with infrared differential interference contrast optics, using a Hamamatsu ORCA-Flash 4.0 complementary metal-oxide semiconductor camera. Whole-cell recordings were obtained from prefrontal layer 2/3 pyramidal cells with patch pipettes (Harvard Apparatus; GC150F-10; outer diameter, 1.5 mm; inner diameter, 0.86 mm; 10 cm length) filled with standard intracellular solution [95 mM K-gluconate, 50 mM KCl, 10 mM Hepes, 4 mM Mg-ATP, 0.5 mM Na-GTP, 10 mM phosphocreatine, and 2% biocytin; (pH 7.2) KOH-adjusted, 300 mOsm]. Electrophysiological recordings were made using MultiClamp700B amplifiers (Molecular Devices, Sunnyvale, CA). Signals were filtered at 10 kHz using Bessel filter and digitized (50 kHz) with a Digidata 1440A and pCLAMP 10 (Molecular Devices, Sunnyvale, CA). Series resistance was monitored, and recordings were discarded if the series resistance changed significantly or reached 20 megaohm. Pyramidal cells were identified by their morphology and action potential spiking properties. Spontaneous voltage clamp–recorded traces were analyzed using Mini Analysis Program (Synaptosoft Inc.).

For measurements of main biophysical parameters [resting membrane potential, input resistance and capacitance, action potential (AP) firing threshold, maximal AP frequency, and AP half-width] after adolescent microglia depletion, 51 pyramidal cells from seven PBS mice and 53 pyramidal cells from seven CDS mice were included. In this cohort of animals, 26 pyramidal cells from three mice per treatment group were included for measurements of sIPSCs, whereas 35 pyramidal cells from four PBS mice and 27 pyramidal cells from four CDS mice were included for measurements of sEPSCs. For measurements of main biophysical parameters after preadolescent microglia depletion, 68 pyramidal cells from eight PBS mice and 69 pyramidal cells from eight CDS mice were included. In this cohort of animals, 33 pyramidal cells from eight mice per treatment group were included for measurements of sIPSCs, whereas 28 pyramidal cells from eight PBS mice and 29 pyramidal cells from eight CDS mice were included for measurements of sEPSCs. For measurements of main biophysical parameters after adult microglia depletion, 69 pyramidal cells from eight PBS mice and 73 pyramidal cells from eight CDS mice were included. In this cohort of animals, 29 pyramidal cells from eight PBS mice and 28 pyramidal cells from eight CDS mice were included for measurements of sEPSCs, whereas 26 pyramidal cells from seven PBS mice and 20 pyramidal cells from seven CDS mice were included for measurements of sIPSCs. To avoid spurious findings arising from pseudoreplication, the number of animals (rather than the number of cells) was considered as the experimental unit in all statistical analyses of electrophysiological data (see below).

After electrophysiological recordings, the slices were fixed with 4% paraformaldehyde (PFA) in 0.1 M PBS overnight. They were then transferred to 0.1 M PBS and washed three times for 10 min on a shaker at room temperature. After washing, the slices were incubated for 48 hours with streptavidin Alexa Fluor 488 conjugate (dilution 1:500; S32354, Thermo Fisher Scientific, Switzerland) in 0.1 M PBS containing 1% Triton X-100 at 4°C. The slices were then washed again three times in 0.1 M PBS for 10 min on a shaker at room temperature and coverslipped with VECTASHIELD mounting medium (H-1000-10, Vector Laboratories).

Immunohistochemistry

The animals were deeply anesthetized with an overdose of pentobarbital (Esconarkon ad us. vet., Streuli Pharma AG, Switzerland) and transcardially perfused with 20 ml of ice-cold PBS followed by 60 ml of ice-cold 4% phosphate-buffered PFA with a perfusion rate of 20 ml/min. The brains were immediately removed from the skull and postfixed in 4% PFA for 6 hours before cryoprotection in 30% sucrose in PBS for 48 hours. The brains were cut coronally with a sliding microtome at 30 μm (eight serial sections) and stored at −20°C in cryoprotectant solution [50 mM sodium phosphate buffer (pH 7.4) containing 15% glucose and 30% ethylene glycol; Sigma-Aldrich, Switzerland] until further processing.

Immunofluorescent stainings were performed according to previously established protocols (*51*, *52*, *58*, *59*). Briefly, the brain sections were rinsed in tris buffer (pH 7.4) before incubating with primary antibodies. A summary of all antibodies used for the immunohistochemical experiments is provided in Table 1 (primary antibodies) and Table 2 (secondary antibodies). The primary antibodies were diluted in tris buffer containing 0.2% Triton X-100 and 2% normal serum. The sections were incubated free-floating under constant agitation (100 rpm) overnight at 4°C. The following day, sections were washed three times for 10 min in tris buffer before a 30-min incubation period with secondary antibodies diluted in tris buffer containing 2% normal serum at room temperature. After incubation, which was shielded from light, the sections were washed 3 × 10 min in tris buffer, mounted onto gelatinized glass slides, coverslipped with Dako fluorescence mounting medium (S3023, Agilent, Switzerland), and stored in the dark at 4°C until image acquisition (see below).

Microscopy and immunofluorescent image analyses

Assessment of cell numbers

Immunofluorescence (IF)–stained images of $Iba1^+$ microglia, neuronal nuclei–positive ($NeuN^+$) neurons, and S100 calcium-binding protein β–positive ($S100\beta^+$) astrocytes were acquired with a widefield microscope (Axio Observer Z1, Zeiss, Jena, Germany) using a 10× [air; numerical aperture (NA), 0.3] objective. Consecutive tile scans of whole coronal brain sections were captured (bregma: +2.2 mm, +1.8 mm, +1.4 mm, and +0.5 mm) and exported from the ZEN Software as tiff format. Cell numbers within the regions of interest (medial PFC, primary motor cortex, secondary motor cortex, primary somatosensory cortex, and forceps minor of the corpus callosum) were counted using the particle analyzer plugin for the ImageJ software. The threshold for each marker was set to acquire optimal representation of microglia, neurons, and astrocytes and kept constant during image analyses. Microglia, neuron, and astrocyte cell numbers were normalized to each individual area of interest and displayed as cells per square millimeter. All analyses were conducted by an experimenter who was blinded to the treatment conditions in the form of numerical codes.

Estimation of synaptic density via colocalization analysis

Double-IF images of VGLUT1 and PSD-95 (excitatory synapses) or VGAT and Gephyrin (inhibitory synapses) were taken using sequential acquisition of separate wavelength channels by confocal laser scanning microscopy (Leica DMI6000 AFC, Model SP8, Mannheim, Germany) with a 63× (oil, NA 1.4) objective and a zoom of 1.8. Laser intensities for each channel were set and kept constant during the entire image acquisition. For each animal, 12 single-plane images were randomly acquired from four consecutive sections containing the PFC (bregma: +2.2 to +1.4 mm). Colocalization between $VGLUT1^+$ and $PSD\text{-}95^+$ puncta (excitatory synapses) or VGAT and Gephyrin (inhibitory synapses) was measured and calculated using a custom-made macro (provided by J.-M. Fritschy, Institute of Pharmacology and

Table 1. List of primary antibodies used for immunohistochemistry. Wherever applicable, the table specifies the vendor, description, catalog number (Cat#), and dilution of the primary antibodies used for immunohistochemistry. The selected antibodies have been validated thoroughly in previous studies using C57BL6/N mice (*51*, *58*, *59*). n.a., not applicable.

Target	Vendor	Description, Cat#	Dilution
Alpha-1 subunit of the inhibitory $GABA_A$ receptor (Gabra1)	Custom-made*	Rabbit polyclonal, n.a.	1:10,000
Bassoon	Enzo Life Sciences	Mouse monoclonal, ADI-VAM-PS003	1:1000
Gephyrin	Synaptic Systems, Germany	Mouse monoclonal, 147 011	1:1000
Ionized calcium-binding adaptor molecule 1 (Iba1)	FUJIFILM Wako Chemicals, USA	Rabbit polyclonal, 019-19741	1:3000
Neuronal nuclei (NeuN)	Synaptic Systems, Germany	Guinea pig polyclonal, 266 004	1:1000
Postsynaptic density protein 95 (PSD-95)	Thermo Fisher Scientific, Switzerland	Mouse monoclonal, MA1-046	1:1000
S100 calcium-binding protein β (S100β)	Abcam, The Netherlands	Rabbit monoclonal, ab52642	1:1000
Vesicular glutamate transporter 1 (VGLUT1)	Synaptic Systems, Germany	Guinea pig polyclonal, 135 304	1:1000
Vesicular inhibitory amino acid transporter (VGAT)	Synaptic Systems, Germany	Rabbit polyclonal, 131 002	1:1000

*The primary antibody against Gabra1 was custom-made by J.-M. Fritschy, Institute of Pharmacology and Toxicology, University of Zürich, Switzerland. Its production and validation have been described previously (*19*).

Toxicology, University of Zürich, Switzerland) developed for the ImageJ software. This macro has been extensively validated for immunohistochemical colocalization studies and has been described in detail previously (*51*, *58*). Briefly, Gaussian filter, background subtraction, and a threshold were applied to the images for each channel. The settings for each marker were adjusted so that an optimal representation of VGLUT1, PSD-95, VGAT, and Gephyrin was achieved and kept constant during image analyses. The number of colocalized clusters was defined as pixel clusters in the presynaptic channel (VGLUT1 or VGAT) that overlapped with pixel clusters in the postsynaptic channel (PSD-95 or Gephyrin), with a set size cutoff at 0.05 μm^2.

Sholl analysis

The complexity of dendritic arbors of biocytin-labeled layer 2/3 pyramidal neurons of the PFC was assessed by means of the Sholl analysis (*60*). Images were captured with confocal laser scanning microscopy (Leica DMI6000 AFC, Model SP8, Mannheim, Germany) using a 20× (oil, NA 0.75) objective with a minimal z-stack distance of 2 μm. All images were deconvolved with Huygens Professional version 20.10 (Scientific Volume Imaging, The Netherlands, http://svi.nl), using the CMLE algorithm, with SNR:10 and 40 iterations. After deconvolution, the images were imported into Imaris image analysis software (version 9.6.0, Oxford Instruments). Neurons were reconstructed three-dimensionally using the "filament creation" wizard. Manual error correction was performed to ensure accurate dendrite rendering. For the Sholl analysis, a sphere radius gap of 20 μm was chosen, and the number of dendrite intersections against the radial distance from soma was quantified automatically by the software. On average, five to six pyramidal neurons per animal were included in the Sholl analysis. To avoid spurious findings arising from pseudoreplication, the number of animals (N = 7 to 8 per treatment) was considered as the experimental unit in statistical analyses (see below).

Classification and quantification of dendritic spines

Dendritic spines were classified and quantified for biocytin-labeled layer 2/3 pyramidal neurons of the PFC. Image acquisition was performed with confocal laser scanning microscopy (Leica DMI6000 AFC, Model SP8, Mannheim, Germany) using a 63× (oil, NA 1.4) objective with a zoom of 3 and a minimal z-stack distance of 0.5 μm. All images were deconvolved with Huygens Professional version 20.10 (Scientific Volume Imaging, The Netherlands, http://svi.nl), using the CMLE algorithm, with SNR:10 and 40 iterations. After deconvolution, the images were imported into Imaris image analysis software (version 9.6.0, Oxford Instruments). Dendrites of layer 2/3 pyramidal cells in the PFC were surface-rendered using the semiautomated "autopath" algorithm in the filament creation wizard. Whenever necessary, manual error correction was performed to obtain a full representation of the individual dendrites with the corresponding spines. The "classify spines Xtension" function was used with default parameters to classify different spine classes (filopodia, long-thin, mushroom, and stubby spines). Spines with a length shorter than 1 μm were classified as stubby, whereas spines with a length shorter than 3 μm and a mean spine head width larger than the doubled mean neck width were classified as mushroom. Spines with a mean spine head width larger or equal the mean spine neck width were classified as long thin. Spines that did not match the previous criteria were classified as filopodia. The number of spines per 100-μm dendrite was analyzed for each spine class. These analyses were conducted by an experimenter who was blinded to the treatment conditions in the form of numerical codes. For each animal, four dendritic sections (each ranging 80 to 90 μm in length) of four distinct pyramidal neurons per animal were included for the quantification of dendrites. Hence, a total length of 320 to 360 μm per animal was included in the analysis of dendritic spines. To avoid spurious findings arising from pseudoreplication, the number of animals (N = 7 to 8 per treatment) was considered as the experimental unit in statistical analyses (see below).

Estimation of synaptic particles within microglia

Double-IF images of $Iba1^+$ microglia and $Bassoon^+$ synaptic particles were taken using sequential acquisition of separate wavelength channels by confocal laser scanning microscopy (Spinning disk, Visitron CSU-W1, Visitron Systems, Puchheim, Germany) with a

Table 2. List of secondary antibodies used for immunohistochemistry.

Host species	Target species	Conjugate	Distributor	Cat#	Dilution
Goat	Rabbit	Alexa Fluor 488	Thermo Fisher Scientific, Switzerland	A-11008	1:500
Goat	Guinea pig	Cy3	Jackson ImmunoResearch Laboratories, Europe Ltd	106-165-003	1:500
Donkey	Rabbit	Alexa Fluor 488	Jackson ImmunoResearch Laboratories, Europe Ltd	711-545-152	1:500
Donkey	Guinea pig	Cy5	Jackson ImmunoResearch Laboratories, Europe Ltd	706-175-148	1:500
Donkey	Mouse	Cy3	Jackson ImmunoResearch Laboratories, Europe Ltd	715-165-150	1:500

100× (oil, NA 1.4) objective. Laser intensities for each channel were set and kept constant during the entire image acquisition. For each animal, 12 series of images with a minimal z-stack distance of 0.13 μm were randomly acquired from three consecutive sections containing the medial portion of the PFC spanning the IL, PL, and AC subregions (bregma: +2.2 to +1.4 mm). All images were deconvolved with Huygens Professional version 20.10 (Scientific Volume Imaging, The Netherlands, http://svi.nl) using the CMLE algorithm with SNR:10 and 40 iterations. After deconvolution, the images were imported into Imaris image analysis software (version 9.6.0, Oxford Instruments). Iba1$^+$ microglia were reconstructed three-dimensionally using the "surface creation" wizard. Bassoon$^+$ synaptic puncta were generated using the "spots creation" wizard with default parameters. The "split into surface objects" function was used to quantify Bassoon$^+$ synaptic particles within surface-rendered Iba1$^+$ microglia. The colocalizing synaptic particles were normalized to the volume of microglia.

Next-generation RNA-seq

The animals were deeply anesthetized with an overdose of pentobarbital (Esconarkon ad us. vet., Streuli Pharma AG, Switzerland) and transcardially perfused with 20 ml of ice-cold ACSF (pH 7.4) as described previously (*59*). After decapitation, the brains were immediately extracted from the skull, frozen on dry ice, and stored at −80°C until further processing. The brains were then cut into 1-mm coronal brain sections using razorblade cuts, and subsequent microdissection of the medial PFC (bregma: +2.5 to +1.5 mm) was performed as described previously (*51*, *56*). Total RNA was isolated using the SPLIT RNA Extraction Kit (008.48, Lexogen, Vienna, Austria). The procedure was conducted according to the manufacturer's instructions, and the resulting RNA was quantified by Nanodrop (DeNovix DS-11+ spectrophotometer, Labgene Scientific SA, Switzerland). The samples were then stored at −80°C until further use.

RNA integrity and amount were determined using a Bioanalyzer 2100 (Agilent Technologies). Only samples with an RNA integrity number > 8 were further processed and included in the analysis. The TruSeq Stranded Total RNA Library prep kit (Illumina) with ribosomal depletion and dual barcoding [2 × 10 base pairs (bp)] was used to produce library constructs. Briefly, 400 ng of total RNA per sample was ribosomal RNA–depleted, fragmented, and reverse-transcribed into double-stranded cDNA and ligated with adapters. Polymerase chain reaction (PCR) was performed to selectively enrich for fragments containing adapters on both ends. Quality and quantity of enriched libraries were analyzed using a Bioanalyzer 2100 (Agilent Technologies) with a DNA-specific chip. Diluted libraries (10 nM) were pooled and sequenced on an Illumina NovaSeq 6000 (100SR v1, Illumina) to an average depth of ~40 million 100-bp single-end reads per sample.

RNA-seq reads were mapped to mouse genome (GRCm38.p5) with STAR version 2.7.3a (*61*) using the default parameters. We obtained, on average, 83.3% uniquely mapped reads per sample. Reads were assigned to genes with featureCounts (*62*) with the following parameters: -t exon -g gene_id, gene annotation - Gencode GRCm38/vM12. The differential expression analysis was carried out with DESeq2 version 1.22.1 (*63*) using the default parameters. We kept genes that have at least five reads in at least five samples.

Differentially expressed genes (DEGs) were identified by applying an FDR correction set at a 5% threshold ($q < 0.05$). Only genes that passed this FDR threshold were considered as significant DEGs. Gene ontology analysis was carried out using the gseGO function from clusterProfiler package (R/Bioconductor) (*64*). Functional network prediction was generated through the use of QIAGEN's IPA (QIAGEN, Redwood City). IPA uses the curated Ingenuity Knowledge Base to identify the involvement of DEGs in specific diseases and cellular pathways and to establish functional networks of direct and indirect interactions between DEGs based on a functional analysis algorithm (*65*). For IPA, we only considered DEGs that passed the FDR threshold ($q < 0.05$) as describe above.

Single-cell suspensions and flow cytometry

The animals were deeply anesthetized with an overdose of pentobarbital (Esconarkon ad us. vet., Streuli Pharma AG, Switzerland) and transcardially perfused with 20 ml of ice-cold PBS with a perfusion rate of 20 ml/min. The brains were then cut into 1-mm coronal brain sections using razorblade cuts, and subsequent

microdissection of the medial PFC (bregma: +2.5 to +1.5 mm) was performed as described previously (*51*, *56*). The PFC samples were cut into small pieces using razorblade cuts and subsequently incubated with digestion buffer [Hanks' balanced salt solution with Ca^{2+}/Mg^{2+} supplemented with 5% fetal bovine serum, 2 mM Hepes, and collagenase type IV (0.4 mg/ml; catalog no. C4-BIOC, Sigma-Aldrich)] for 45 min at 37°C under constant agitation. The samples were homogenized with a syringe and filtered through a 100-μm cell strainer (15380801, Thermo Fisher Scientific) mounted onto a 50-ml Falcon tube. The filtered samples were mixed with 30% Percoll (17089101, GE Healthcare) in PBS (v/v) and centrifuged at 2700 rpm for 30 min at 4°C without brakes during deceleration. The resulting myelin layer (top white layer) was removed using a suction pump, and the transparent layer with cells of interest was filtered through a 100-μm cell strainer (15380801, Thermo Fisher Scientific). The single-cell suspension was washed in ice-cold PBS and centrifuged at 1500 rpm for 15 min at 4°C to pellet the cells. Cells were then ready for flow cytometry analysis.

To avoid nonspecific binding of antibodies, cells were incubated with anti-mouse CD16/32 (catalog no. 101310, BioLegend) in PBS for 15 min at 4°C to block the Fc receptors. Subsequently, the cells were washed with PBS and resuspended in the antibody mix in PBS. Cell surface staining was performed for 20 min at 4°C. After washing with PBS, cells were resuspended in fluorescence-activated cell sorting buffer (2 mM EDTA and 2% fetal calf serum in PBS) and acquired by an LSRII Fortessa flow cytometer (BD Biosciences). Data analysis was performed using FlowJo version 10.8.0 (Tree Star). Duplets were excluded for analysis using side scatter area/height (SSC-A/H), forward scatter area/height (FSC-A/H), and dead cells by a Fixable Viability Kit (near-infrared staining, catalog no. 423105, BioLegend). All antibodies used for the flow cytometric analyses are specified in the figure legend of fig. S5.

MACS for microglia isolation

Microglia were isolated from the PFC using MACS of cells that were harvested using an optimized mechanical dissociation protocol at 4°C, as validated and described previously (*66*). Briefly, mice were deeply anesthetized with an overdose of pentobarbital (Esconarkon ad us. vet., Streuli Pharma AG, Switzerland) and transcardially perfused with 15 ml of ice-cold calcium- and magnesium-free Dulbecco's PBS (DPBS; 14190144, Thermo Fisher Scientific, Switzerland) via a 20-ml syringe and a 23-gauge needle (25 mm length). The brains were quickly removed and washed with ice-cold DPBS, after which the PFC was dissected on a cooled petri dish and placed in an ice-cold Hibernate-A medium (HAPR, Brainbits). Mechanical dissociation was carried out on ice, while all the solutions were kept at 4°C. The PFC samples of three mice were pooled per data point and were dissociated in 1.5 ml of Hibernate-A medium in a 1-ml Dounce homogenizer (40401, Active Motif) with a loose pestle. The tissue was gently homogenized and then sieved through a 70-μm cell strainer (15370801, Thermo Fisher Scientific) mounted onto a 50-ml Falcon tube. The Dounce homogenizer was washed twice with 1 ml of Hibernate-A, whereby each wash was poured onto the cell strainer. The homogenized PFC samples were then transferred to 5-ml Eppendorf tubes and kept on ice. The homogenates were pelleted at 400*g* for 6 min at 4°C in a swing-bucket rotor centrifuge (Eppendorf, Schönenbuch, Switzerland). The supernatants were removed, and 1 ml of ice-cold DPBS was added to all samples. The pellets were then resuspended with a P1000 micropipette. After resuspension, the final volume in each tube was brought to 1.5 ml. Freshly prepared isotonic percoll solution (500 μl; 17089101, GE Healthcare) was added to each sample and mixed well. Percoll was rendered isotonic by mixing 1 part of 10× calcium- and magnesium-free DPBS (14200075, Thermo Fisher Scientific, Switzerland) with 9 parts of percoll. The pH of percoll was adjusted to 7.3 to 7.4 with 5 M hydrochloric acid before starting the isolation procedure. The percoll solution was mixed properly with the cell suspension, after which 2 ml of DPBS was gently layered on top of it, creating two separate layers. The samples were centrifuged for 10 min at 3000*g*. The centrifugation resulted in an upper layer consisting of DPBS and a lower layer consisting of percoll. The two layers were separated by a disk of myelin and debris, while the cells were located at the bottom of the tube. The layers above the cell pellet were aspirated, leaving about 500 μl. The cells were then washed once in 4 ml of DPBS, making sure not to resuspend the pellet. The cells were then pelleted by centrifugation at 400*g* for 10 min at 4°C.

Microglia were isolated by MACS using mouse anti-CD11b magnetic microbeads (130-093-634, Miltenyi) according to the manufacturer's instructions with some modifications. The MACS buffer used consisted of 1.5% bovine serum albumin (BSA) diluted in DPBS from a commercial 7.5% cell culture–grade BSA stock (Thermo Fisher Scientific, 11500496). For the isolation of microglia, cell pellets were resuspended in 80 μl of MACS buffer and 10 μl of FcR-blocking reagent (Miltenyi). The cells were then incubated for 10 min at 4°C. Thereafter, 10 μl of anti-CD11b magnetic microbeads was added, and the cells were incubated for 15 min at 4°C. The cells were then washed with 1 ml of MACS buffer and pelleted at 300*g* for 5 min at 4°C. The cells were passed through an MS MACS column (130-042-201, Miltenyi) attached to a magnet. This led CD11b-labeled cells to stay attached to the column, whereas unlabeled cells flowed through. After washing the columns three times with MACS buffer, the columns were removed from the magnet, and microglia were eluted with 1 ml of MACS buffer and pelleted at 300*g* for 5 min at 4°C.

Total RNA from the cell pellets was isolated using the SPLIT RNA Extraction Kit (008.48, Lexogen, Vienna, Austria). The procedure was conducted according to the manufacturer's instructions, and the resulting RNA was quantified by Nanodrop (DeNovix DS-11+ spectrophotometer, Labgene Scientific SA, Switzerland). The samples were stored at −80°C until further use [gene expression analyses using quantitative real-time PCR (qRT-PCR); see below].

Quantitative real-time polymerase chain reaction

qRT-PCR was performed according to previously established protocols (*51*, *52*, *54*). RNA was extracted from bulk PFC samples or microglial cells isolated via MACS as described above and was analyzed by a TaqMan qRT-PCR instrument (CFX384 real-time system, Bio-Rad Laboratories) using the iScript one-step qRT-PCR kit for probes (Bio-Rad Laboratories). The samples were run in 384-well formats in triplicates as multiplexed reactions with a normalizing internal control (36B4). Thermal cycling was initiated with an incubation at 50°C for 10 min (RNA retrotranscription) and then at 95°C for 5 min (TaqMan polymerase activation). After this initial step, 39 cycles of PCR were performed. Each PCR cycle consisted of heating the samples at 95°C for 10 s to enable the melting process and then for 30 s at 60°C for the annealing and extension reaction. Relative target gene expression was calculated according to the $2^{-\Delta\Delta Ct}$ method (*67*). Custom-designed probe and primer sequence used for the reference gene (*36B4*) and TaqMan assay IDs for the genes of interest are summarized in Table 3.

Table 3. List of mouse TaqMan gene expression assays used in this study. The list summarizes the names of the genes of interest and their TaqMan assay ID, listed according to alphabetical order. 36B4 was custom-designed, with the following probe and primer sequences.

Gene name	TaqMan assay ID
36B4	Custom-designed*
Allograft inflammatory factor 1 (*Aif1*; = *Iba1*)	Mm00479862_g1
Chemokine (C-X3-C motif) receptor 1 (*Cx3cr1*)	Mm00438354_m1
Colony-stimulating factor 1 receptor (*Csf1r*)	Mm01266652_m1
Complement component 3 (*C3*)	Mm01232779_m1
$GABA_A$ receptor, subunit alpha 1 (*Gabra1*)	Mm00439046_m1
$GABA_A$ receptor, subunit alpha 2 (*Gabra2*)	Mm00433435_m1
$GABA_A$ receptor, subunit alpha 3 (*Gabra3*)	Mm01294271_m1
$GABA_A$ receptor, subunit alpha 5 (*Gabra5*)	Mm00621092_m1
Purinergic receptor P2Y, G protein–coupled 12 (*P2ry12*)	Mm01950543_s1
Pyrimidinergic receptor P2Y, G protein–coupled 6 (*P2ry6*)	Mm02620937_s1
Spi-1 proto-oncogene (*Spi1*; = *Pu.1*)	Mm00488140_m1
Triggering receptor expressed on myeloid cells 2 (*TREM2*)	Mm04209424_g1

**36b4*: primers: 5′-AGATGCAGCAGATCCGCAT-3′ (forward) and 5′-GTTCTTGC CCATCAGCACC-3′ (reverse); probe: 5′-CGCTCCGAGGGAAGGCCG-3′.

Statistical analyses

All statistical analyses of behavioral, immunohistochemical, qRT-PCR, and flow cytometry data were performed using Statistical Package for the Social Sciences (SPSS) Statistics (version 25.0, IBM, Armonk, NY, USA) and Prism (version 8.0; GraphPad Software, La Jolla, California), with statistical significance set at $P < 0.05$ unless specified otherwise. All immunohistochemical data involving three treatment groups (sham, PBS, and CDS) were analyzed using one-way analysis of variance (ANOVA), followed by Tukey's post hoc test for multiple comparisons. All immunohistochemical data involving two treatment groups (PBS and CDS) were analyzed using independent Student's *t* tests (two-tailed), with the exception of the Sholl analysis data, which were analyzed using 2 × 16 (treatment × distance intervals) repeated-measures ANOVA, followed by Tukey's post hoc test for multiple comparisons. All electrophysiological measurements were analyzed using independent Student's *t* tests (two-tailed), whereby the number of animals (rather than the number of cells) was considered as the experimental unit.

All dependent variables in the open-field test (total distance moved, distance moved in the center zone, and the number of center zone visits) and light-dark box test (total distance and time spent in the light compartment) were analyzed using independent Student's *t* tests (two-tailed) as well. In the social interaction test, the social preference index and social memory index were also analyzed using independent Student's *t* tests (two-tailed), whereas the absolute times exploring the live mouse versus inanimate dummy object (phase 1) or exploring the unfamiliar versus familiar mouse (phase 2) were analyzed using 2 × 2 (treatment × object) repeated-measures ANOVA, followed by repeated-measures ANOVA restricted to either treatment group (PBS or CDS) whenever appropriate. In the temporal order memory tests, the temporal order memory index was analyzed using independent Student's *t* tests (two-tailed), whereas the relative amount of time exploring the objects in sample phases 1 and 2 of the test was analyzed using chi-square tests. In the contextual fear conditioning and extinction test, percent time freezing during the habituation and conditioning phases (day 1) was analyzed using 2 × 6 (treatment × bins) and 2 × 9 (treatment × bins) repeated-measures ANOVAs, respectively, whereas percent time freezing during the expression phase (day 2) was analyzed using 2 × 12 (treatment × bins) repeated-measures ANOVAs. The extinction rate was analyzed using 2 × 4 (treatment × days) repeated-measures ANOVAs, followed by Tukey's post hoc for multiple comparisons. Transcriptomic data were analyzed as described above, using FDR correction set at a 5% threshold ($q < 0.05$). Only genes that passed this FDR threshold were considered as significant DEGs.

SUPPLEMENTARY MATERIALS

Supplementary material for this article is available at https://science.org/doi/10.1126/sciadv.abi6672

View/request a protocol for this paper from *Bio-protocol*.

REFERENCES AND NOTES

1. E. Koechlin, C. Ody, F. Kouneiher, The architecture of cognitive control in the human prefrontal cortex. *Science* **302**, 1181–1185 (2003).
2. M. Carlén, What constitutes the prefrontal cortex? *Science* **358**, 478–482 (2017).
3. A. Caballero, R. Granberg, K. Y. Tseng, Mechanisms contributing to prefrontal cortex maturation during adolescence. *Neurosci. Biobehav. Rev.* **70**, 4–12 (2016).
4. M. Chini, I. L. Hanganu-Opatz, Prefrontal cortex development in health and disease: Lessons from rodents and humans. *Trends Neurosci.* **44**, 227–240 (2021).
5. B. Larsen, B. Luna, Adolescence as a neurobiological critical period for the development of higher-order cognition. *Neurosci. Biobehav. Rev.* **94**, 179–195 (2018).
6. N. Gogtay, J. N. Giedd, L. Lusk, K. M. Hayashi, D. Greenstein, A. C. Vaituzis, T. F. Nugent, D. H. Herman, L. S. Clasen, A. W. Toga, J. Rapoport, P. M. Thompson, Dynamic mapping of human cortical development during childhood through early adulthood. *Proc. Natl. Acad. Sci. U.S.A.* **101**, 8174–8179 (2004).
7. T. Sakurai, N. J. Gamo, T. Hikida, S. H. Kim, T. Murai, T. Tomoda, A. Sawa, Converging models of schizophrenia—Network alterations of prefrontal cortex underlying cognitive impairments. *Prog. Neurobiol.* **134**, 178–201 (2015).
8. L. D. Selemon, N. Zecevic, Schizophrenia: A tale of two critical periods for prefrontal cortical development. *Transl. Psychiatry* **5**, e623 (2015).
9. P. J. Harrison, L. Colbourne, C. H. Harrison, The neuropathology of bipolar disorder: Systematic review and meta-analysis. *Mol. Psychiatr.* **25**, 1787–1808 (2020).
10. S. A. Wolf, H. W. Boddeke, H. Kettenmann, Microglia in physiology and disease. *Annu. Rev. Physiol.* **79**, 619–643 (2017).
11. L. J. Lawson, V. H. Perry, P. Dri, S. Gordon, Heterogeneity in the distribution and morphology of microglia in the normal adult mouse brain. *Neuroscience* **39**, 151–170 (1990).
12. M. Mittelbronn, K. Dietz, H. J. Schluesener, R. Meyermann, Local distribution of microglia in the normal adult human central nervous system differs by up to one order of magnitude. *Acta Neuropathol.* **101**, 249–255 (2001).
13. D. P. Schafer, E. K. Lehrman, A. G. Kautzman, R. Koyama, A. R. Mardinly, R. Yamasaki, R. M. Ransohoff, M. E. Greenberg, B. A. Barres, B. Stevens, Microglia sculpt postnatal neural circuits in an activity and complement-dependent manner. *Neuron* **74**, 691–705 (2012).
14. A. R. Bialas, B. Stevens, Retracted article: TGF-β signaling regulates neuronal C1q expression and developmental synaptic refinement. *Nat. Neurosci.* **16**, 1773–1782 (2013).
15. L. Cheadle, S. A. Rivera, J. S. Phelps, K. A. Ennis, B. Stevens, L. C. Burkly, W. A. Lee, M. E. Greenberg, Sensory experience engages microglia to shape neural connectivity through a non-phagocytic mechanism. *Neuron* **108**, 451–468.e9 (2020).

16. L. Weinhard, G. di Bartolomei, G. Bolasco, P. Machado, N. L. Schieber, U. Neniskyte, M. Exiga, A. Vadisiute, A. Raggioli, A. Schertel, Y. Schwab, C. T. Gross, Microglia remodel synapses by presynaptic trogocytosis and spine head filopodia induction. *Nat. Commun.* **9**, 1228 (2018).
17. R. C. Paolicelli, G. Bolasco, F. Pagani, L. Maggi, M. Scianni, P. Panzanelli, M. Giustetto, T. A. Ferreira, E. Guiducci, L. Dumas, D. Ragozzino, C. T. Gross, Synaptic pruning by microglia is necessary for normal brain development. *Science* **333**, 1456–1458 (2011).
18. A. P. Mallya, H.-D. Wang, H. N. R. Lee, A. Y. Deutch, Microglial pruning of synapses in the prefrontal cortex during adolescence. *Cereb. Cortex* **29**, 1634–1643 (2019).
19. F. Ginhoux, M. Greter, M. Leboeuf, S. Nandi, P. See, S. Gokhan, M. F. Mehler, S. J. Conway, L. G. Ng, E. R. Stanley, I. M. Samokhvalov, M. Merad, Fate mapping analysis reveals that adult microglia derive from primitive macrophages. *Science* **330**, 841–845 (2010).
20. K. Kierdorf, D. Erny, T. Goldmann, V. Sander, C. Schul, E. G. Perdiguero, P. Wieghofer, A. Heinrich, P. Riemke, C. Hölscher, D. N. Müller, B. Luckow, T. Brocker, K. Debowski, G. Fritz, G. Opdenakker, A. Diefenbach, K. Biber, M. Heikenwalder, F. Geissmann, F. Rosenbauer, M. Prinz, Microglia emerge from erythromyeloid precursors via Pu.1- and Irf8-dependent pathways. *Nat. Neurosci.* **16**, 273–280 (2013).
21. C. N. Parkhurst, G. Yang, I. Ninan, J. N. Savas, J. R. Yates III, J. J. Lafaille, B. L. Hempstead, D. R. Littman, W. B. Gan, Microglia promote learning-dependent synapse formation through brain-derived neurotrophic factor. *Cell* **155**, 1596–1609 (2013).
22. T. Masuda, L. Amann, R. Sankowski, O. Staszewski, M. Lenz, P. D. Errico, N. Snaidero, M. J. Costa Jordão, C. Böttcher, K. Kierdorf, S. Jung, J. Priller, T. Misgeld, A. Vlachos, M. Meyer-Luehmann, K. P. Knobeloch, M. Prinz, Novel Hexb-based tools for studying microglia in the CNS. *Nat. Immunol.* **21**, 802–815 (2020).
23. M. R. Elmore, A. R. Najafi, M. A. Koike, N. N. Dagher, E. E. Spangenberg, R. A. Rice, M. Kitazawa, B. Matusow, H. Nguyen, B. L. West, K. N. Green, Colony-stimulating factor 1 receptor signaling is necessary for microglia viability, unmasking a microglia progenitor cell in the adult brain. *Neuron* **82**, 380–397 (2014).
24. L. Torres, J. Danver, K. Ji, J. T. Miyauchi, D. Chen, M. E. Anderson, B. L. West, J. K. Robinson, S. E. Tsirka, Dynamic microglial modulation of spatial learning and social behavior. *Brain Behav. Immun.* **55**, 6–16 (2016).
25. P. P. Lehenkari, M. Kellinsalmi, J. P. Näpänkangas, K. V. Ylitalo, J. Mönkkönen, M. J. Rogers, A. Azhayev, H. K. Väänänen, I. E. Hassinen, Further insight into mechanism of action of clodronate: Inhibition of mitochondrial ADP/ATP translocase by a nonhydrolyzable, adenine-containing metabolite. *Mol. Pharmacol.* **61**, 1255–1262 (2002).
26. C. M. Drzewiecki, J. Willing, J. M. Juraska, Synaptic number changes in the medial prefrontal cortex across adolescence in male and female rats: A role for pubertal onset. *Synapse* **70**, 361–368 (2016).
27. L. K. Bicks, H. Koike, S. Akbarian, H. Morishita, Prefrontal cortex and social cognition in mouse and man. *Front. Psychol.* **6**, 1805 (2015).
28. G. R. Barker, F. Bird, V. Alexander, E. C. Warburton, Recognition memory for objects, place, and temporal order: A disconnection analysis of the role of the medial prefrontal cortex and perirhinal cortex. *J. Neurosci.* **27**, 2948–2957 (2007).
29. S. Maren, K. L. Phan, I. Liberzon, The contextual brain: Implications for fear conditioning, extinction and psychopathology. *Nat. Rev. Neurosci.* **14**, 417–428 (2013).
30. K. P. Berry, E. Nedivi, Spine dynamics: Are they all the same? *Neuron* **96**, 43–55 (2017).
31. G. Choii, J. Ko, Gephyrin: A central GABAergic synapse organizer. *Exp. Mol. Med.* **47**, e158 (2015).
32. J. M. Fritschy, H. Mohler, GABAA-receptor heterogeneity in the adult rat brain: Differential regional and cellular distribution of seven major subunits. *J. Comp. Neurol.* **359**, 154–194 (1995).
33. E. Bertoss, C. Tesini, A. Cappelli, E. Ciaramelli, Ventromedial prefrontal damage causes a pervasive impairment of episodic memory and future thinking. *Neuropsychologia* **90**, 12–24 (2016).
34. O. Y. Chao, M. A. de Souza Silva, Y. M. Yang, J. P. Huston, The medial prefrontal cortex - hippocampus circuit that integrates information of object, place and time to construct episodic memory in rodents: Behavioral, anatomical and neurochemical properties. *Neurosci. Biobehav. Rev.* **113**, 373–407 (2020).
35. B. Delatour, P. Gisquet-Verrier, Involvement of the dorsal anterior cingulate cortex in temporal behavioral sequencing: Subregional analysis of the medial prefrontal cortex in rat. *Behav. Brain Res.* **126**, 105–114 (2001).
36. D. K. Hannesson, G. Vacca, J. G. Howland, A. G. Phillips, Medial prefrontal cortex is involved in spatial temporal order memory but not spatial recognition memory in tests relying on spontaneous exploration in rats. *Behav. Brain Res.* **153**, 273–285 (2004).
37. N. M. Dudukovic, A. D. Wagner, Goal-dependent modulation of declarative memory: Neural correlates of temporal recency decisions and novelty detection. *Neuropsychologia* **45**, 2608–2620 (2007).
38. A. Caballero, E. Flores-Barrera, D. K. Cass, K. Y. Tseng, Differential regulation of parvalbumin and calretinin interneurons in the prefrontal cortex during adolescence. *Brain Struct. Funct.* **219**, 395–406 (2014).
39. D. K. Cass, E. Flores-Barrera, D. R. Thomases, W. F. Vital, A. Caballero, K. Y. Tseng, CB1 cannabinoid receptor stimulation during adolescence impairs the maturation of GABA function in the adult rat prefrontal cortex. *Mol. Psychiatry* **19**, 536–543 (2014).
40. J. H. Kim, R. Richardson, A developmental dissociation of context and GABA effects on extinguished fear in rats. *Behav. Neurosci.* **121**, 131–139 (2007).
41. J. H. Kim, A. S. Hamlin, R. Richardson, Fear extinction across development: The involvement of the medial prefrontal cortex as assessed by temporary inactivation and immunohistochemistry. *J. Neurosci.* **29**, 10802–10808 (2009).
42. E. C. King, S. S. Pattwell, C. E. Glatt, F. S. Lee, Sensitive periods in fear learning and memory. *Stress* **17**, 13–21 (2014).
43. M. G. Cunningham, S. Bhattacharyya, F. M. Benes, Amygdalo-cortical sprouting continues into early adulthood: Implications for the development of normal and abnormal function during adolescence. *J. Comp. Neurol.* **453**, 116–130 (2002).
44. T. Chan, K. Kyere, B. R. Davis, A. Shemyakin, P. A. Kabitzke, H. N. Shair, G. A. Barr, C. P. Wiedenmayer, The role of the medial prefrontal cortex in innate fear regulation in infants, juveniles, and adolescents. *J. Neurosci.* **31**, 4991–4999 (2011).
45. A. Waisman, F. Ginhoux, M. Greter, J. Bruttger, Homeostasis of microglia in the adult brain: Review of novel microglia depletion systems. *Trends Immunol.* **36**, 625–636 (2015).
46. R. Hanamsagar, M. D. Alter, C. S. Block, H. Sullivan, J. L. Bolton, S. D. Bilbo, Generation of a microglial developmental index in mice and in humans reveals a sex difference in maturation and immune reactivity. *Glia* **65**, 1504–1520 (2017).
47. V. Mondelli, A. C. Vernon, F. Turkheimer, P. Dazzan, C. M. Pariante, Brain microglia in psychiatric disorders. *Lancet Psychiatry* **4**, 563–572 (2017).
48. E. Parellada, P. Gassó, Glutamate and microglia activation as a driver of dendritic apoptosis: A core pathophysiological mechanism to understand schizophrenia. *Transl. Psychiatry* **11**, 271 (2021).
49. M. Germann, S. G. Brederoo, I. E. C. Sommer, Abnormal synaptic pruning during adolescence underlying the development of psychotic disorders. *Curr. Opin. Psychiatry* **34**, 222–227 (2021).
50. M. S. Keshavan, J. Giedd, J. Y. Lau, D. A. Lewis, T. Paus, Changes in the adolescent brain and the pathophysiology of psychotic disorders. *Lancet Psychiatry* **1**, 549–558 (2014).
51. T. Notter, S. M. Schalbetter, N. E. Clifton, D. Mattei, R. Richetto, K. Thomas, U. Meyer, J. Hall, Neuronal activity increases translocator protein (TSPO) levels. *Mol. Psychiatry* **26**, 2025–2037 (2021).
52. M. Schalbetter, F. S. Mueller, J. Scarborough, J. Richetto, U. Weber-Stadlbauer, U. Meyer, T. Notter, Oral application of clozapine-N-oxide using the micropipette-guided drug administration (MDA) method in mouse DREADD systems. *Lab. Anim* **50**, 69–75 (2021).
53. M. A. Labouesse, W. Langhans, U. Meyer, Abnormal context-reward associations in an immune-mediated neurodevelopmental mouse model with relevance to schizophrenia. *Transl. Psychiatry* **5**, e637 (2015).
54. J. Richetto, M. A. Labouesse, M. M. Poe, J. M. Cook, A. A. Grace, M. A. Riva, U. Meyer, Behavioral effects of the benzodiazepine-positive allosteric modulator SH-053-2'F-S-CH_3 in an immune-mediated neurodevelopmental disruption model. *Int. J. Neuropsychopharmacol.* **18**, pyu055 (2015).
55. U. Weber-Stadlbauer, J. Richetto, M. A. Labouesse, J. Bohacek, I. M. Mansuy, U. Meyer, Transgenerational transmission and modification of pathological traits induced by prenatal immune activation. *Mol. Psychiatry* **22**, 102–112 (2017).
56. F. S. Mueller, J. Scarborough, S. M. Schalbetter, J. Richetto, E. Kim, A. Couch, Y. Yee, J. P. Lerch, A. C. Vernon, U. Weber-Stadlbauer, U. Meyer, Behavioral, neuroanatomical, and molecular correlates of resilience and susceptibility to maternal immune activation. *Mol. Psychiatry* **26**, 396–410 (2021).
57. C. Belzung, G. Griebel, Measuring normal and pathological anxiety-like behaviour in mice: A review. *Behav. Brain Res.* **125**, 141–149 (2001).
58. T. Notter, J. M. Coughlin, T. Gschwind, U. Weber-Stadlbauer, Y. Wang, M. Kassiou, A. C. Vernon, D. Benke, M. G. Pomper, A. Sawa, U. Meyer, Translational evaluation of translocator protein as a marker of neuroinflammation in schizophrenia. *Mol. Psychiatry* **23**, 323–334 (2018).
59. T. Notter, P. Panzanelli, S. Pfister, D. Mircsof, J. M. Fritschy, A protocol for concurrent high-quality immunohistochemical and biochemical analyses in adult mouse central nervous system. *Eur. J. Neurosci.* **39**, 165–175 (2014).
60. K. E. Binley, W. S. Ng, J. R. Tribble, B. Song, J. E. Morgan, Sholl analysis: A quantitative comparison of semi-automated methods. *J. Neurosci. Methods* **225**, 65–70 (2014).
61. A. Dobin, C. A. Davis, F. Schlesinger, J. Drenkow, C. Zaleski, S. Jha, P. Batut, M. Chaisson, T. R. Gingeras, STAR: Ultrafast universal RNA-seq aligner. *Bioinformatics* **29**, 15–21 (2013).
62. Y. Liao, G. K. Smyth, W. Shi, featureCounts: An efficient general purpose program for assigning sequence reads to genomic features. *Bioinformatics* **30**, 923–930 (2014).
63. M. I. Love, W. Huber, S. Anders, Moderated estimation of fold change and dispersion for RNA-seq data with DESeq2. *Genome Biol.* **15**, 550 (2014).
64. G. Yu, L. G. Wang, Y. Han, Q. Y. He, clusterProfiler: An R package for comparing biological themes among gene clusters. *OMICS* **16**, 284–287 (2012).

65. S. Thomas, D. Bonchev, A survey of current software for network analysis in molecular biology. *Hum. Genomics* **4**, 353–360 (2010).
66. D. Mattei, A. Ivanov, M. van Oostrum, S. Pantelyushin, J. Richetto, F. Mueller, M. Beffinger, L. Schellhammer, J. Vom Berg, B. Wollscheid, D. Beule, R. C. Paolicelli, U. Meyer, Enzymatic dissociation induces transcriptional and proteotype bias in brain cell populations. *Int. J. Mol. Sci.* **21**, 7944 (2020).
67. K. J. Livak, T. D. Schmittgen, Analysis of relative gene expression data using real-time quantitative PCR and the 2−ΔΔCT method. *Methods* **25**, 402–408 (2001).
68. J. D. Cahoy, B. Emery, A. Kaushal, L. C. Foo, J. L. Zamanian, K. S. Christopherson, Y. Xing, J. L. Lubischer, P. A. Krieg, S. A. Krupenko, W. J. Thompson, B. A. Barres, A transcriptome database for astrocytes, neurons, and oligodendrocytes: A new resource for understanding brain development and function. *J. Neurosci.* **28**, 264–278 (2008).
69. Y. Zhang, K. Chen, S. A. Sloan, M. L. Bennett, A. R. Scholze, S. O'Keeffe, H. P. Phatnani, P. Guarnieri, C. Caneda, N. Ruderisch, S. Deng, S. A. Liddelow, C. Zhang, R. Daneman, T. Maniatis, B. A. Barres, J. Q. Wu, An RNA-sequencing transcriptome and splicing database of glia, neurons, and vascular cells of the cerebral cortex. *J. Neurosci.* **34**, 11929–11947 (2014).
70. T. R. Hammond, C. Dufort, L. Dissing-Olesen, S. Giera, A. Young, A. Wysoker, A. J. Walker, F. Gergits, M. Segel, J. Nemesh, S. E. Marsh, A. Saunders, E. Macosko, F. Ginhoux, J. Chen, R. J. M. Franklin, X. Piao, S. A. McCarroll, B. Stevens, Single-cell RNA sequencing of microglia throughout the mouse lifespan and in the injured brain reveals complex cell-state changes. *Immunity* **50**, 253–271 (2019).

Acknowledgments: We thank S. Kreutzer and G. Russo from the Functional Genomics Center Zürich (FGCZ), Switzerland, for technical assistance in RNA-seq. Imaging was performed with equipment maintained by the Center for Microscopy and Image Analysis, University of Zürich. Specifically, we would like to express our gratitude toward P. Schätzle for technical support in imaging. **Funding:** This work was supported by the Swiss National Science Foundation (grant no. 310030_188524) awarded to U.M. Additional support was received from a Postdoc Mobility grant (grant no. P2ZHP3_174868) awarded to T.N. by the Swiss National Science Foundation and by a "Postdoc-Forschungskredit" grant (FK-20-067) awarded to F.S.M. by the University of Zürich (UZH). **Author contributions:** S.M.S., A.S.v.A., N.C.-O., K.D., A.I., F.S.M., H.-Y.L., R.A., W.M., and D.M. were involved in acquisition, analysis, and interpretation of the study data; S.M.S., D.B., C.F., M.G., T.N., and U.M. were involved in the conception and design of the study and analysis and interpretation of the study data; C.F., M.G., T.N., and U.M. supervised the research; S.M.S., T.N., and U.M. wrote the initial manuscript draft; all authors contributed to reviewing and editing of the manuscript and have given final approval for the version to be published. **Competing interests:** The authors declare that they have no competing interests. **Data and materials availability:** All data needed to evaluate the conclusions in the paper are present in the paper and/or the Supplementary Materials. The RNA-seq data discussed in this publication have been deposited in NCBI's Gene Expression Omnibus and are accessible through GEO Series accession number GSE168268 (https://ncbi.nlm.nih.gov/geo/query/acc.cgi?acc=GSE168268).

Submitted 23 March 2021
Accepted 5 January 2022
Published 2 March 2022
10.1126/sciadv.abi6672